NORTHWESTERN UNIVERSITY

Modeling of Oscillations and Bursting in Retinal AII Amacrine Cells

A DISSERTATION

SUBMITTED TO THE GRADUATE SCHOOL

IN PARTIAL FULFILLMENT OF THE REQUIREMENTS

for the degree

DOCTOR OF PHILOSOPHY

Field of Applied Mathematics

By

Hannah Choi

EVANSTON, ILLINOIS

August 2014

ABSTRACT

Modeling of Oscillations and Bursting in Retinal AII Amacrine Cells

Hannah Choi

The goal of this thesis is to elucidate the mechanisms responsible for various dynamics displayed by the AII amacrine (AII) cell, with particular emphasis on bursting generated by individual AIIs. Chapter 1 introduces the overarching ideas and reviews key concepts of the thesis, providing general overviews on the AII amacrine cell, the rod bipolar pathway, and the characteristic oscillations observed in photoreceptor-degenerated retina. It also covers previous studies on the transition between bursting and spiking in various models. Chapters 2 and 3 discuss the mechanisms of experimentally observed firing patterns in AII cells based on simulations with a physiologically realistic compartmental model of the AII.

Chapter 2 probes the origin of the characteristic oscillations with a frequency of $\sim$ 10-15 Hz observed in the degenerated retina. In collaboration with experimentalists, electrophysiological and computational methods were combined to demonstrate that the oscillations are generated by the intrinsic membrane properties of individual AII cells and share the same mechanism with bursting observed in hyperpolarized wildtype AII cells.

Specifically, the oscillations are cable-filtered bursts that arise from interactions of fast Na and A-type K currents with a slow M-type K current. The significance of the slow M-type K current in generation of the oscillations is predicted by the model and then confirmed by experiments.

Chapter 3 employs bifurcation theory to explain the mechanism underlying bursting in the compartmental AII model. By decoupling the fast subsystem from the slow subsystem, we show that the bursting mechanism relies on the hysteresis between limit cycles and fixed points, which lose stability via saddle-node bifurcations. The full system of the AII model is considered in order to understand a transition between tonic spiking and bursting. The transition involves a torus bifurcation and exhibits a range of bistability, where both tonic spiking and bursting coexist.

Acknowledgements

First of all, I would like to thank my advisors, Professors Hermann Riecke and William Kath, for their patience and wisdom with which they have guided me through my graduate school years. I sincerely appreciate their dedication and assistance. They have been always there to help, support, and guide me. I have learned so much from their mentorship and feel extremely fortunate to have had this experience with them as my advisors. I also thank their wives, Marge and Bonnie, for inviting me to summer barbecues and a Thanksgiving dinner.

I also would like to thank Professor David Chopp, for being on my thesis committee and reviewing the thesis even with his extremely busy schedule. I am deeply grateful for his time and devotion.

I thank our collaborators from University of Maryland. Without them, I would never have been able to appreciate neuroscience research fully. I thank Professor Joshua Singer for his insights, patience, and guidance. I would also like to thank Lei Zhang, Carl Sabottke, and Alex Markowitz. Lei performed all the experiments on intracellular recordings; Carl and Alex did the extracellular recordings. I thank them for numerous emails we have exchanged. Even when I asked them the most basic questions on experiments, they were always willing to answer and help me understand their works. Through interacting and working with them, I have learned the joy of collaborative research.

Many thanks to Mark Cembrowski, who has helped me a lot with his experiences and knowledge. Even after he left Northwestern, he has been always willing to help whenever I had questions on various things ranging from the very basics of retina to NEURON modeling. Also, thanks to Lucie, for reading and commenting on my abstract.

I appreciate the friends that I made these past five years at Northwestern. Without them I would never have been able to make this road through. I will always remember my time here with so many fond memories I made with them. I feel very fortunate that I have met such outstanding people. Thank you for all the wonderful moments. Those times with friends are the best part of my years here.

I am grateful to my family for their love and supports. I thank my parents for being always encouraging and supportive. I also thank my brother Kiri for being such an awesome brother. Thank you for always being there for me. Finally, I thank my grandmother for her love, strength, and prayers. I dedicate this thesis to my loving grandmother.

Table of Contents

List of Figures

CHAPTER 1

Introduction

Mathematical modeling has solved many interesting problems in neuroscience. With the rapid advance in experimental techniques, physiologically realistic modeling based on experimental data is becoming increasingly valuable, as it provides comprehensive insights into neuronal systems. Mathematical modeling can provide meaningful predictions for neuronal behavior and functionality, thus helping experimental designs. At the same time, modeling can also deliver more in-depth explanations of experimental results. For example, neuronal modeling allows one to explore the variables in the neural system that cannot be measured experimentally.

This thesis utilizes mathematical modeling of the AII amacrine cell, a class of retinal interneurons that play a central role in the rod bipolar pathway, to elucidate the mechanisms underlying characteristic oscillations that arise under pathological conditions. Furthermore, it explores different dynamic patterns of the cell, namely tonic spiking and bursting, by studying their bifurcation structures. The rest of the introduction first reviews past studies that have motivated the works included in this thesis. Then it delivers the motivation and the organization of the thesis.

1.1. The AII amacrine cell plays a central role in the rod bipolar pathway

The retina has developed two distinct pathways, one involving cones and the other involving rods, in order to operate over a broad range of light intensity from moonless

nights to bright days. Cone photoreceptors have high thresholds and do not saturate under bright light stimuli, and thus mediate photopic vision. The rods are highly sensitive to light, but their responses saturate quickly when there are more photons. Therefore, the rods mediate scotopic vision when the light level is near the absolute threshold for vision [**23**]. In the mammalian retina, rod signals are known to be transmitted through three different pathways (Figure 1.1, [**23**]). First, the rod-cone pathway employs the cones and the cone bipolar cells to transmit the rod signals to the ganglion cells, through the electrical coupling between the rods and the cones [**49, 54**]. In the second pathway, termed the rod-OFF pathway, rods make synaptic contacts with OFF-cone bipolar cells, which in turn relay the rod input to the ganglion cells [**59, 30**]. However, the primary route for rod signal transmission is the rod bipolar pathway. In the rod bipolar pathway, the signals from rods are passed on to rod bipolar cells (RBs) via excitatory glutamatergic synapses [**22, 53**]. The rod bipolar cells then relay these signals to a network of electrically coupled AII amacrine cells, also via glutamatergic synapses [**19**]. AII amacrine cells are electrically coupled to ON-cone bipolar (ONCB) cells [**72**], which transmit the signals to ON ganglion cells [**26**]. AII amacrine cells also make inhibitory glycinergic synapses onto OFF ganglion cells [**44, 70**]. Both ON and OFF retinal ganglion cells (RGCs) are the retinal output cells, which send the signals to the brain. Thus, the AII amacrine cell mediates both ON and OFF pathways, and scotopic signals must pass through the AIIs first before leaving the retina for higher brain regions. In other words, the AII amacrine cell plays a central role in the rod bipolar pathway.

Due to its essential role in the rod bipolar pathway, the AII amacrine cell has received significant attention. The biophysical properties of the AII have been investigated in

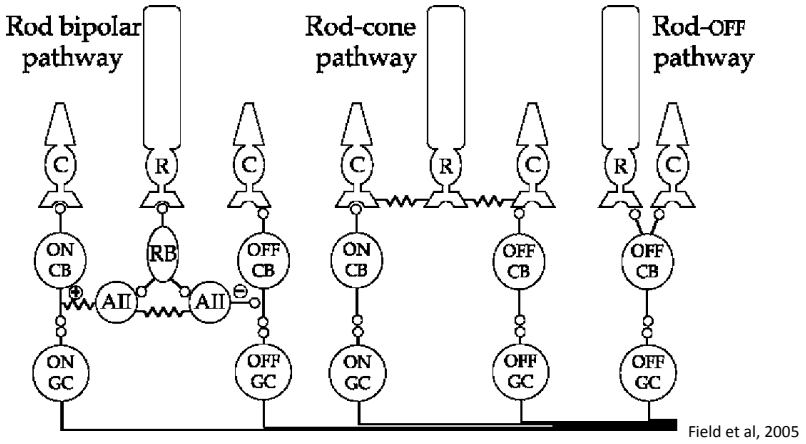

Figure 1.1. **Rod signal pathways**
Rod signals are transmitted through the rod bipolar pathway, the rod-cone pathway, and the rod-OFF pathway. The figure is taken from Field et al, 2005 [**23**].

many previous studies. The AII is known to possess a Na conductance— in particular, the Nac1.1 subunit [**36**]. Three different types of K channels have been identified to be in the AII: a high voltage-activated A-type K conductance [**66**], a non-inactivating M-type K conductance [**14**], and a Ca-activated K conductance [**28**]. L-type Ca channels, which are believed to mediate chemical synaptic release, were also shown to be localized to lobules presynaptic to OFF cone bipolar and ganglion cells [**29**]. The AII amacrine cell is an unconventional neuron in terms of its structure; it is an axonless neuron and has only a soma and elaborate dendrites (Figure 1.2). It has an asymmetric dendrite protruding from the body, with a small lobule attached to it. It has been shown in a recent work [**14**] that this lobule is the spike initiation site which is electrotonically distal from the rest of the AII cell. Electrophysiological experiments and simulations using a compartmental model of the AII have indicated that the electrotonically distal single initiation site has a Na and an M-type K conductances, and is responsible for the small amplitude (< 10mV)

spontaneous tonic spiking observed in the AII cells [**14**]. It has been also shown that under a hyperpolarizing current injection, the spontaneously spiking wildtype AII cell undergoes a transition to bursting mediated by the M-type K current.

AIIs are electrically coupled to other AIIs [**71**] as well as to ONCBs [**72**] via gap junctions. The gap junction coupling to both ONCBs and other AIIs occur at the dendrites of the AII. The coupling strengths between AIIs and ONCBs range from 100 pS to 1,500 pS for type 5, 6, and 7 ONCB cells [**72**]. The electrical coupling strength between AIIs, however, is modulated by ambient illumination [**8**]. In dark-adapted retinas, AII cells are coupled relatively weakly, but at the illumination corresponding to twilight, the coupling increases and the effective size of the coupled network of AII cells increases as a consequence. Further light-adaptation decreases the coupling strengths, to values similar to the coupling strengths under the dark-adapted condition. The strong AII-AII coupling under dim background lights has been suggested to provide for summation of synchronous activity over a wider area and thus to preserve the fidelity of the rod-driven signals [**58**].

1.2. Oscillations in the degenerated retina

Retinitis pigmentosa collectively refers to retinal degeneration where photoreceptors progressively die, starting with cones. The rd1 mouse is a well-studied mouse model for this type of retinal degeneration. In the rd1 mouse, the photoreceptors progressively die in the first weeks after birth. The remaining retinal circuitry, however, appears to stay largely intact for quite some time [**43**], and starts to exhibit spontaneous rhythmic activities with a frequency in the range ∼5-15 Hz. Such oscillatory activities are found in both ON and OFF ganglion cells[**60, 46**].

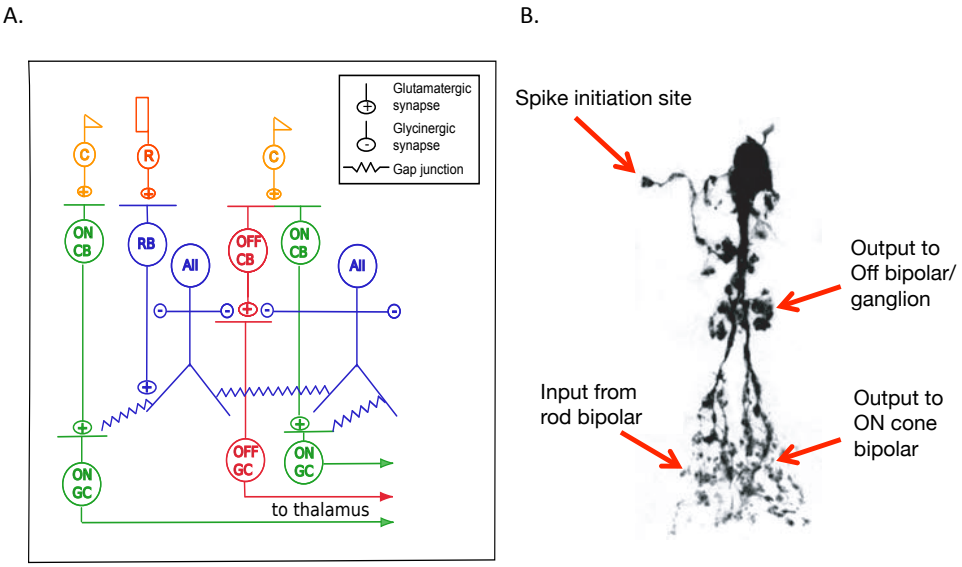

Figure 1.2. **The rod bipolar pathway and the AII amacrine cell**
A. The rod bipolar pathway. **B.** A confocal image of an AII amacrine cell.

Many studies have sought the origin of these oscillations. Previous studies indicate that the oscillations come from the cells upstream to the ganglion cells, as the oscillatory activities in RGCs were eliminated in the presence of synaptic blockers and such oscillations are observed in AII amacrine cells and ONCBs as well [**46, 9, 47, 60, 76, 77**].

The precise origin of the rd oscillations, however, has not been identified. In [**77**], independent dystrophied amacrine cells were implicated to drive the oscillations. In this study, non-NMDA and NMDA glutamate receptor blockers did not eliminate oscillatory inhibitory post-synaptic currents (IPSCs) in the RGCs and the oscillations in the amacrine

cells, indicating that the bipolar cells are not the source of the rd oscillations. The inhibitory transmission was necessary for rd oscillations in the RGCs, suggesting that the amacrine cells are the source of the rd oscillations. In addition to abolishing the rd oscillations, blocking inhibitory receptors uncovered distinct slow Ca-dependent oscillations in the RGCs, which originate in the bipolar cells. Moreover, the IPSC oscillations in the RGCs were shown to persist in the presence of the gap junction blocker carbernoxolone (CBX), which led to a conclusion that gap junctions may not be necessary to generate the oscillations.

In [**47**], however, the local field potentials (LFPs) in the rd retina, which is believed to reflect the rhythmic activities in the RGCs, persisted in the presence of the Na blocker tetrodotoxin (TTX) and inhibitory receptor antagonists, but were eliminated under the application of ionotrophic glutamate receptor blockers. Furthermore, application of gap junction blockers CBX and meclofenamic acid (MFA) both abolished the LFPs. The observation that glutamate release in the presence of functional electrical synapses is required for the LFPs point to the cells presynaptic to RGCs as the generator of the rd oscillations. Since the Na blocker TTX did not eliminate the rd1 LFPs [**47**] and the rhythmic activity of amacrine cells require Na [**46, 9**], the bipolar cells were hypothesized as the likely source of the rd oscillations. However, many other studies [**9, 68, 46, 45**] including the experiments from the Singer laboratory have observed the elimination of the rd oscillations under TTX application. The discrepancy between these studies and [**47**] may have come from the use of different TTX concentrations.

In other studies [**9, 68**], the gap-junction coupled network of AII amacrine cells and ON cone bipolar cells has been implicated as the source of these oscillations. In [**68**], the rd

oscillations of ∼10-20 Hz were observed in both ONCBs and the AII amacrine cells. These oscillations were abolished by application of the Na channel blocker TTX. Since voltage-gated Na channels were only observed in AII amacrine cells, but not in ONCBs, it was suggested that the AII amacrine cells are the major drivers of the oscillations. Moreover, as in [**47**], application of the gap junction blocker MFA eliminated the rd oscillations in the network of AII-ONCB cells. Based on these observations, it was hypothesized that the gap junction coupling between the AII amacrine cells is necessary for generation of the rd oscillations, and the oscillations arise from the network effect of slightly heterogeneous AII amacrine cells that are electrically-coupled to each other.

A recent study [**45**] further supports that the rd oscillations in the RGCs arise from the upstream AII amacrine cell inputs. While the like-pairs of alpha RGCs, namely, ON/ON and OFF/OFF pairs, exhibited the bursts of action potentials in phase, bursting in ON and OFF alpha ganglion cells was anti-correlated. As the AII amacrine cells provide correlated indirect excitation to ON RGCs and direct inhibition to OFF RGCs, this result is consistent with the notion that the rhythmic activities observed in the RGCs of the rd1 retina originate from the AII amacrine cells.

It is worth noting that the oscillations similar to the rd1 oscillations have been observed in the wildtype retina as well. It has been shown that in wildtype (wt) retina, blocking the photoreceptor inputs to bipolar cells induced oscillatory activities in the AII-ONCB cell network following a hyperpolarization by about 10mV [**68**]. In accordance with this observation, in [**14**], a hyperpolarizing current injection to the AII amacrine cell induced spontaneous bursting in the cell, which were similar in frequency and waveform to the rd oscillations in AII amacrine cells.

The rd oscillations may have some functional impact on the signal processing in the remaining retinal structure. To treat retinitis pigmentosa and similar retinal degenerations, various strategies to render some of the remaining cells photosensitive have been pursued [**50**]. Indeed, cell transplantation [**41**], gene therapy [**1**], biological [**7, 39, 37, 11**] and electronic implants [**73, 62**] have had remarkable success in restoring some aspects of sight in animals and even in humans with retinal degeneration. However, the efficiency of the transmission of the signals that arise from such prosthesis or remaining cones can be greatly reduced due to the rd oscillations [**77, 67**]. Light-evoked (photoreceptor cell-dependent) activity driven by remaining cone photoreceptors were markedly less effective in transmitting evoked responses compared to the wildtype retina [**77**]. More importantly, even when a current pulse was delivered to the inner nuclear layer, bypassing photoreceptors, the transmission of electrically evoked signals was significantly exacerbated in the rd1 retina compared to the wildtype retina, demonstrating that synaptic noise in rd retina can reduce the effectiveness of signal transmission [**77**]. In rd10 mouse, another mouse model for retinal degeneration which shows later onset of photoreceptor degeneration compared to the rd1 mouse, the majority of RGCs were spontaneously bursting, but a small subset of quiescent RGCs could be identified as well. By comparing the light responses originating from the remaining photoreceptors in the bursting and the quiescent RGCs, it has been shown that the spontaneous bursting activity masks the light responses. Moreover, blocking of the aberrant bursting by application of the gap junction blocker MFA restored light sensitivity [**67**]. Taken together, these studies support that removing the rd oscillations may be an important target for treatments for the retinal

degeneration. In order to achieve it, it is critical to understand the precise origin and the mechanism of the rd oscillations.

1.3. Transition between bursting and spiking

Tonic spiking and bursting are dynamic patterns most commonly observed in neuronal activity. Each mode of firing plays different functional roles in many neural systems and a transition from one pattern to another may have significant functional impacts. For example, bursting is observed in pathological brain states such as epileptic seizure [**61, 65, 5, 4**]. The transition from spiking to bursting in neural systems can be investigated by studying the bifurcation structure of the neuronal model. The transition can involve quite complex bifurcation structures, and past studies have developed multiple scenarios describing the transition between tonic spiking and bursting .

In a model of the leech heartbeat neuron studied in [**57**], the transition between tonic spiking and bursting involves blue sky catastrophes. There, the spiking state terminates in a saddle-node (fold) bifurcation which creates a bursting state with infinitely long active phase in the form of an orbit homoclinic to the saddle-node of periodic orbits. In such a bifurcation, the transition between the tonic spiking and bursting regimes are continuous and reversible.

The tonic spiking state can also change to the bursting state via a non-smooth transition. For example, the spiking state can lose stability in either a torus (also called Neimark-Sacker or secondary Hopf) bifurcation or a period doubling bifurcation which involves cascades to chaos [**74, 63, 64**].

Moreover, it has been shown that the transition from spiking to bursting can involve torus canards [**10, 6**], where the uniform amplitude tonic spiking loses stability via a torus bifurcation, followed by amplitude modulated spiking and then to the bursting state via a torus canard explosion. Here, the transition from spiking to bursting occurs by a torus bifurcation in the full system. In the fast subsystem, the limit cycles loses the stability via a fold, and the system follows the unstable limit cycles for some time, resulting in the amplitude modulation.

In some cases, the transition between tonic spiking and bursting involves hysteresis. Coexistence of a tonic spiking mode and a bursting mode has been observed in modeling [**12, 56, 18, 27**] as well as in experiments [**32, 38, 69**]. Such multistability has various potential implications for different neural systems, motivating investigation of the underlying mechanism of bistability between tonic spiking and bursting in various neuronal models.

In [**56**], the coexistence of tonic spiking and bursting is explained by averaging the slow equations, as introduced by Pontryagin and Rodygin [**52**]. Namely, for the model studied in [**56**], the averaged function for the rate of the slow variable change determines whether the system exhibits tonic spiking or bursting and also explains the coexistence. More specifically, the Lukyanov-Shilnikov bifurcation of a saddle-node periodic orbit with homoclinics gives a rise to the bistability. In this study, a reduced model of a leech heart interneuron, a system of three differential equations for the voltage, a sodium inactivation variable, and a persistent potassium current activation variable, exhibits tonic spiking and bursting coexisting for a certain range of a control parameter. Whether the model shows tonic spiking or bursting depends on the initial state. In this model, the K activation

m_{k2} is the slow phase variable, and the voltage v and the Na inactivation h_{Na} are the fast ones. The fast subsystem of the model, with the slow parameter continuation, shows that the stable limit cycle branch emerges via a supercritical Hopf bifurcation, and loses the stability via a saddle-node bifurcation. The unstable limit cycle branch then terminates at a homoclinic bifurcation on the unstable fixed points. In order to understand the bistability of spiking and bursting, the rate of change in the slow variable direction was averaged over the surface composed of limit cycles. Namely, the slow variable m_{k2} in this system was described by the differential equation

$$\dot{m}_{k2} = \epsilon G(v, m_{k2}),$$

and the averaged slow equation on the limit cycle branch in the first order of ϵ was calculated by

$$\langle m'_{k2} \rangle = \langle G(v, m_{k2}) \rangle,$$

where $\langle G \rangle$ denotes G averaged over the period of each limit cycle. When $\langle G \rangle$ decreases and crosses 0 once as in Figure1.3A2, the zero of $\langle G \rangle$ becomes the attracting limit cycle, and the system shows tonic spiking only. When $\langle G \rangle$ makes two zeros before the fold of the limit cycle manifold as in Figure1.3B2, one of the zeros is an attracting limit cycle and the other is an unstable limit cycle. The limit cycle manifold is then divided into two parts, and the system exhibits either tonic spiking or bursting depending on the initial state. When the stable and unstable limit cycles get close and annihilate, the model shows bursting only (Figure1.3C, D)[**56, 18, 55**].

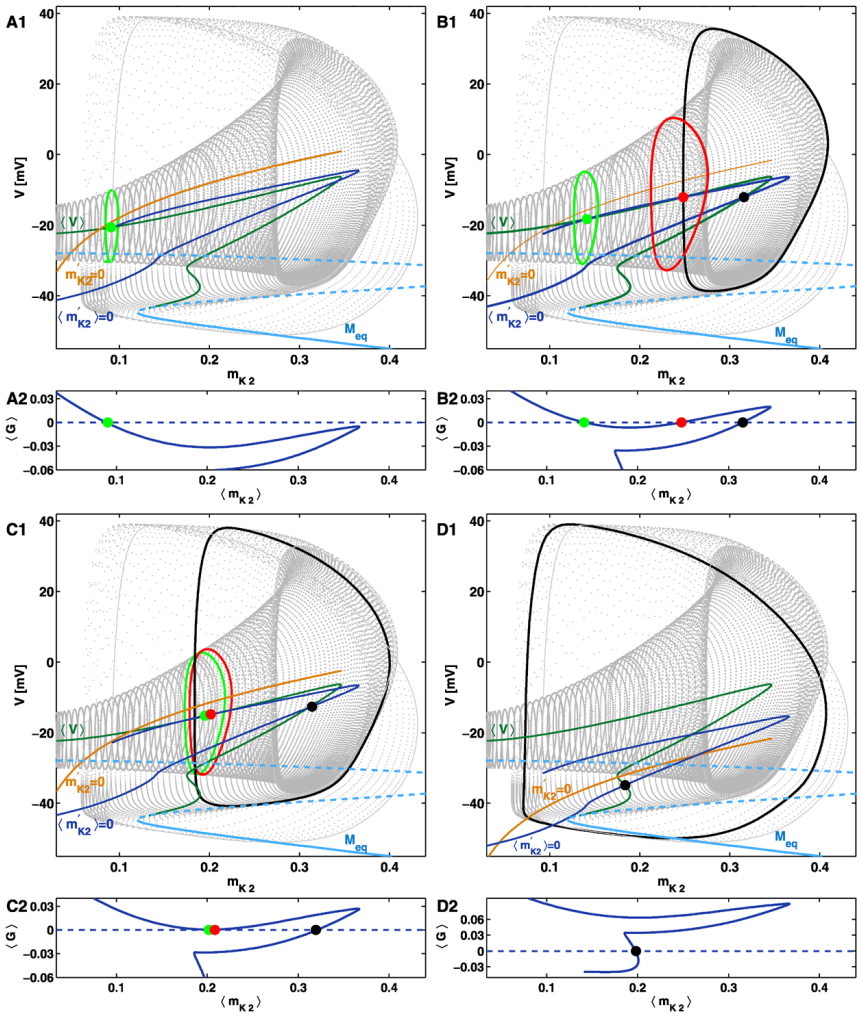

Figure 1.3. **Coexistence of tonic spiking and bursting in a leech heart neuron model is explained by the average slow equation in [55].**
Depending on the trajectory of $\langle G \rangle$, the model exhibits either tonic spiking **A1, A2**, bursting **D1, D2**, or coexistence of bursting and tonic spiking **B1, B2** which disappears when the stable and the unstable periodic orbits coalesce **C1, C2**. The figure is taken from Shilnikov, 2012 [**55**].

In [**27**], on the other hand, the coexistence of tonic spiking and bursting in a model of a cortical pyramidal cell for elevated extracellular potassium concentration is explained by the different levels of deinactivation of the slow parameter in the fast subsystem. In this two-compartmental model of the pyramidal cell, the bifurcation diagram of the decoupled fast subsystem was investigated with the maximum Ca-activated K conductance g_{KCa} as the bifurcation parameter. The bistability of tonic spiking and bursting occurs because of the small range of $g_{KCa} \geq 0$ where stable limit cycles exist. Depending on the initial conditions, when the trajectory is on the stable limit cycles, the model exhibits tonic firing, and when the trajectory alternates between the upper stable fixed points and the lower state fixed points, it generates bursting (Figure 1.4). However, in this study, bursting was classified as alternation between a hyperpolarized state and prolonged depolarization (depolarization block) with quickly occasioning several spikes at the beginning, and it is thus different from the bursting in [**56, 18, 55**], where it is defined as alternation between spiking and quiescent states.

1.4. Motivation and organization of dissertation

The functional extent of the AII amacrine cell has been a focus of interest for its significant role as a central interneuron in the rod bipolar pathway. In the wildtype retina, individual AII amacrine cells show spontaneous tonic spiking. However, the wildtype AII generates bursting when the cell is hyperpolarized. On the other hand, in the rd1 retina, AII amacrine cells exhibit characteristic oscillations with a frequency of $\sim 10 - 15$Hz.

In Chapter 2, we combine experiments and modeling to unravel the mechanism underlying the characteristic oscillations in the rd1 retina. Our compartmental model of AII

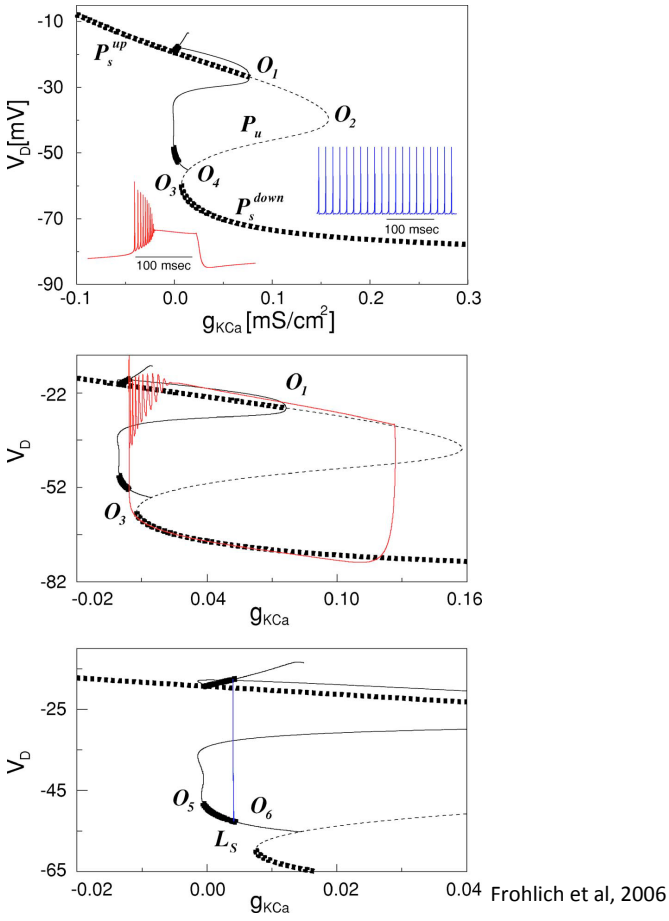

Figure 1.4. **Coexistence of tonic spiking and bursting in a cortical pyramidal neuron model is explained by different levels deinactivation of the slow parameter in [27].**
The fast subsystem at the external potassium concentration $[K^+]_o = 5.9$ mM where the tonic spiking and bursting modes coexist. Thick dashed line indicates stable fixed points, thin dashed line represents unstable fixed points, thick solid line indicates stable limit cycles, and thin solid line represents unstable limit cycles. The middle panel shows the phase trajectory during bursting, and the bottom panel shows tonic firing. The figure is taken from Frohlich et al, 2006 [**27**].

cell predicts that the rd1 oscillations are generated by the same mechanism as bursting in the wildtype AII. The oscillations originate from cable-filtered bursts generated by interplay between fast, Na and A-type K currents and a slow M-type K current. The

model of the AII predicts effects of M-type K current activators and inhibitors on the oscillations. These predictions are then experimentally confirmed, both in the AII cells and the ganglion cells, attesting our hypothesis that the rd1 oscillations are generated by the intrinsic mechanism of individual AIIs, where the M-type K current plays a significant role as the slow modulator.

Chapter 3 further explores the mechanism of bursting as well as the transition between tonic spiking and bursting in the compartmental model of AII, using continuation software XPPAUT and MATCONT. First, fast-slow analysis is employed to reveal that the bursting arises from the hysteresis between a limit cycle branch and a fixed point branch in the fast subsystem. Both the limit cycles and the fixed points become unstable via fold bifurcations. Extending our analysis to the full system allows us to find a torus bifurcation involved in the transition between tonic spiking and bursting and existence of a bistability range in the M-type K conductance where tonic spiking and bursting coexist. Whether the AII model gets attracted to the tonic spiking mode or the bursting mode can be determined by analyzing the averaged slow system.

CHAPTER 2

Mechanism of characteristic oscillations in degenerated rd1 retina

In retinitis pigmentosa, which collectively refers to retinal degeneration where photoreceptors progressively die, inner retinal circuits remain intact. In the rd1 mouse, an established model for blinding retinal diseases, spontaneous activity in the coupled network of AII amacrine and ON cone bipolar cells leads to rhythmic bursting of ganglion cells. Since such activity could impair retinal and/or cortical responses to restored photoreceptor function, understanding its nature is important for developing treatments of retinal pathologies. Here we analyzed a compartmental model of the wild-type mouse AII amacrine cell to predict that the cell's intrinsic membrane properties — specifically, interacting fast Na and slow, M-type K conductances — would allow its membrane potential to oscillate when light-evoked excitatory synaptic inputs were withdrawn following photoreceptor degeneration. This hypothesis was tested and confirmed experimentally in the Singer lab by recording from AIIs in a slice preparation of rd1 retina. Additionally, recordings from ganglion cells in a whole-mount preparation of rd1 retina demonstrated that activity in AIIs was propagated unchanged to elicit bursts of action potentials in ganglion cells. We conclude that oscillations are not an emergent property of a degenerated retinal network. Rather, they arise largely from the intrinsic properties of a single retinal interneuron, the AII amacrine cell.

2.1. Introduction

Retinitis pigmentosa (RP) refers to a collection of retinal diseases in which photoreceptors die (rods followed by cones) [**2, 31**]. Mutations in the β-subunit of rod cGMP-phosphodiesterase occur both in human RP and in mouse models of the disease [**15, 16, 31**]. The rd1 mouse is an established model of RP specifically and of blinding retinal disorders generally [**13, 35**].

Ganglion cells in rd1 retinas are driven to fire bursts of action potentials by phasic synaptic inputs arriving at $\sim$10 Hz [**42, 46, 60**]. Because oscillatory activity might inhibit normal retinal responses to restored photoreceptor function or might inhibit cortical responses to restored visual input by inducing maladaptive changes in visual circuits, interest in elucidating the circuitry generating it has grown. Speaking to the importance of understanding circuit changes following vision loss, restoration of photo-responsiveness in a blind human patient did not restore visual perception [**24**].

The synaptic drive underlying ganglion cell bursting likely originates in the network of electrically coupled AII amacrine cells and ON cone bipolar cells [**9, 68**]. This notion is supported by the observation that bursting in ON and OFF alpha ganglion cells is anti-correlated [**45**], just as light-evoked synaptic excitation to these cell types is anti-correlated in the normal retina [**48**]); the AII network generates this anti-correlation by providing simultaneously indirect excitation to ON alpha cells and direct inhibition to OFF alpha cells [**20**].

Here, we demonstrate that oscillations in the rd1 retina arise from intrinsic membrane properties of AIIs; they are not an emergent property of a network of coupled neurons with heterogeneous intrinsic electrical properties, as has been suggested [**68**]. Specifically,

we tested the hypothesis that AIIs in the rd1 retina are hyperpolarized relative to their wild-type counterparts and that this hyperpolarization permits an interaction between a fast, depolarizing Na conductance and a slow, hyperpolarizing, M-type K conductance to generate phasic bursting, just as it does in the wild-type retina [**14**].

A model of the AII [**14**] allowed us to predict effects of M-type K current activators and inhibitors on oscillations observed experimentally during whole-cell recordings from AIIs in a retinal slice preparation. Experiments performed in the Singer lab showed that pharmacologically-induced alterations in AIIs activities were propagated unchanged to ganglion cells, as revealed by whole-cell recordings from individual cells and by multi-electrode array recordings of population activity. We conclude that the intrinsic properties of rd1 and wild-type AIIs need not differ; rather, hyperpolarization arising from reduced light-dependent synaptic input is sufficient to unmask bursting. Electrical coupling is relevant only because it affects AIIs' membrane potentials. Our finding indicates that treatment of retinal degeneration might benefit from preventing hyperpolarization of AIIs. Inducing light sensitivity in ON bipolar cells [see [**37**]] may accomplish this.

2.2. Methods

Here, the method for the computational modeling used by the author is included. In addition, a brief summary on methods for the experiments performed by the Singer laboratory and the Butts laboratory is included in order to provide a complete picture. For details on the experimental methods, see [**17**].

2.2.1. Computational model

All numerical simulations were performed with MATLAB using ode45, a variable step Runge-Kutta method.

2.2.1.1. Three-compartment model of AII amacrine cell. For the AII we used the three-compartment model from [**14**], which behaves similarly to a morphologically realistic model as shown in [**14**] (Figure 2.4A(i)(ii)). The morphologically detailed model was built based on an AII filled with a fluorescent tracer (Figure 2.4A(i)). Na-, A-type K- and slowly activating M-type K-conductances were inserted into the distal varicosity; the long neurite and the soma were taken to be passive, and the rest of the cell had a low-density A-type K conductance [**14**]. The previous study has shown that, in the morphologically detailed model, voltage responses to a brief current injection at the distal varicosity were very similar when measured in the soma, the lobules at the end of the primary dendrite, and the arboreal dendrite [**14**]. Thus, excepting the distal varicosity that was shown to be the spike-initiation site [**14**] and the attached long neurite, when spiking the rest of the AII behaves as if it is electrotonically compact. This justifies treating the soma and arboreal dendrite as a single compartment.

Specifically, our AII model consisted of a large compartment (length = 25 μm, diameter = 25 μm) representing the soma and arboreal dendrite of the AII, a thin cable-like compartment (length = 32 μm, diameter = 0.3 μm) that represents the long neurite branching from the primary dendrite, and the small initiation site (length = 2 μm, diameter = 2 μm), as shown in Figure 2.4A(ii). For convenience, we will call the large compartment the "soma", the thin cable compartment the "cable", and the small varicosity compartment the "initiation site". Unlike in [**14**], here we treated the cable as one

compartment instead of eleven compartments, after confirming that it does not make a significant difference. In all three compartments, there was a passive leak conductance, with membrane resistivity of 40,000 Ωcm^2. The specific membrane capacitance and axial resistivity were 1 μF cm^{-2} and 150 Ωcm respectively. Therefore, with r_L as the axial resistivity and a_j and l_j as the radius and the length of the compartment j, the resistance between the compartment j and the neighboring compartment j+1 was given by

$$R_{j,j+1} = \frac{r_L}{2\pi}\left(\frac{l_i}{a_j^2} + \frac{l_{j+1}}{a_{j+1}^2}\right), \tag{2.1}$$

and the conductance between the two compartments $\bar{g}_{j,j+1}$ was given by

$$\bar{g}_{j,j+1} = \frac{1}{R_{j,j+1}} \text{ for } j = 1, 2. \tag{2.2}$$

Then, the current from the neighboring compartment was described by

$$i_{compart} = \begin{cases} \bar{g}_{j,j+1}\left(V_{j+1} - V_j\right) & \text{if } j = 1, \\ \bar{g}_{j,j+1}\left(V_{j+1} - V_j\right) + \bar{g}_{j-1,j}\left(V_{j-1} - V_j\right) & \text{if } j = 2, \\ \bar{g}_{j-1,j}\left(V_{j-1} - V_j\right), & \text{if } j = 3, \end{cases} \tag{2.3}$$

where $j = 1, 2, 3$ refers to the soma, the cable, and the initiation site compartment of the AII model, respectively.

In addition, the initiation site had a fast Na conductance ($\bar{g}_{IS,Na} = 0.2$ S/cm^2), an incompletely inactivating A-type K conductance ($\bar{g}_{IS,A} = 0.08$ S/cm^2), and a slow noninactivating M-type K conductance ($\bar{g}_{IS,M} = 0.03$ S/cm^2), as this single distal initiation site has been shown to be the site of spike generation as well as of its slow modulation [**14**].

Although the soma itself was found to be passive [**66**], since the somatic compartment of the three-compartment model was taken to include arboreal dendrites, an A-type K conductance was included in this compartment ($\bar{g}_{soma,A} = 0.004$ S/cm^2). These active conductances, with the reversal potentials $E_{Na} = 50$ mV and $E_K = -77$ mV, had the following kinetics.

The Na current was given by

$$i_{Na} = \bar{g}_{Na} m_{Na}^3 h_{Na} (V - E_{Na}) \tag{2.4}$$

where the activation variable and the inactivation variable were governed by

$$\tau_{m_{Na}} \frac{dm_{Na}}{dt} = m_{\infty,Na} - m_{Na}, \tag{2.5}$$

$$\tau_{h_{Na}} \frac{dh_{Na}}{dt} = h_{\infty,Na} - h_{Na} \tag{2.6}$$

with

$$m_{\infty,Na}(V) = \left[1 + \exp\left(-\frac{(V - V_{1/2,m_{Na}})}{k_{m_{Na}}}\right)\right]^{-1}, \tag{2.7}$$

$$h_{\infty,Na}(V) = \left[1 + \exp\left(\frac{(V - V_{1/2,h_{Na}})}{k_{h_{Na}}}\right)\right]^{-1}, \tag{2.8}$$

where $V_{1/2,m_{Na}} = -48\,\text{mV}$, $k_{m_{Na}} = 5\,\text{mV}$, $V_{1/2,h_{Na}} = -49.5\,\text{mV}$, $k_{h_{Na}} = 2\,\text{mV}$. Both activation and inactivation of the Na current were fast, with time constants $\tau_{m_{Na}} = 0.01\,\text{ms}$ and $\tau_{h_{Na}} = 0.5\,\text{ms}$, respectively.

The M-type K current was given by

$$i_M = \bar{g}_M m_M (V - E_K) \tag{2.9}$$

where the activation variable was described as

$$\tau_{m_M}\frac{dm_M}{dt} = m_{\infty,M} - m_M \tag{2.10}$$

with

$$m_{\infty,M}(V) = \left[1 + \exp\left(-\frac{(V - V_{1/2,m_M})}{k_{m_M}}\right)\right]^{-1}, \tag{2.11}$$

where $V_{1/2,m_M} = -40\,\mathrm{mV}$, $k_{m_M} = 4\,\mathrm{mV}$. The M-type K current is noninactivating, and activates slowly with a time constant $\tau_{m_M} = 50\,\mathrm{ms}$.

Finally, the A-type K current was given by

$$i_A = \bar{g}_A m_A \left(c\, h_A^{(1)} + (1-c)h_A^{(2)}\right)(V - E_K), \tag{2.12}$$

$$c = \left[1 + \exp\left(-\frac{(V+45)}{15}\right)\right]^{-1}, \tag{2.13}$$

where the activation and inactivation variables were governed by

$$\tau_{m_A}\frac{dm_A}{dt} = m_{\infty,A} - m_A, \tag{2.14}$$

$$\tau_{h_A^{(1)}}\frac{dh_A^{(1)}}{dt} = h_{\infty,A} - h_A^{(1)}, \tag{2.15}$$

$$\tau_{h_A^{(2)}}\frac{dh_A^{(2)}}{dt} = h_{\infty,A} - h_A^{(2)} \tag{2.16}$$

with

$$m_{\infty,A}(V) = \left[1 + \exp\left(-\frac{(V - V_{1/2,m_A})}{k_{m_A}}\right)\right]^{-1}, \tag{2.17}$$

$$h_{\infty,A}(V) = f\left[1 + \exp\left(\frac{(V - V_{1/2,h_A})}{k_{h_A}}\right)\right]^{-1} + (1 - f), \tag{2.18}$$

where $V_{1/2,m_A} = -10\,\mathrm{mV}$, $k_{m_A} = 7\,\mathrm{mV}$, $V_{1/2,h_A} = -40.5\,\mathrm{mV}$, $k_{h_A} = 2\,\mathrm{mV}$, and $f = 0.83$. The A-type K current had a relatively fast activation with $\tau_{m_A} = 1\,\mathrm{ms}$ along with a fast inactivation $h_A^{(1)}$ and a slow inactivation $h_A^{(2)}$. Inactivation was incomplete as captured by f in the steady-state expression above, with time scales

$$\tau_{h_A^{(1)}}(V) = 25 - 20\left[1 + \exp\left(-\frac{(V + 35)}{6}\right)\right]^{-1}, \tag{2.19}$$

$$\tau_{h_A^{(2)}}(V) = \min\left\{\frac{(V + 17)^2}{4} + 26,\, 100\right\}. \tag{2.20}$$

The parameters for the A-type K conductance were well-constrained by voltage clamp recordings [**66**], while other parameters were fit to reproduce the experimentally observed spikelets and bursts in wild type AIIs [**14**]. In this three-compartment AII model, we omitted an L-type Ca conductance that is present in AII cells [**29**] since it was not needed to reproduce realistic AII responses in the regime of interest.

The leak current was given by

$$i_{leak} = \bar{g}_{leak}\,(V - E_{leak})\,, \tag{2.21}$$

where $\bar{g}_{leak}$ and E_{leak} are the leak conductance and the leak reversal potential, respectively. When the AII cell is electrically coupled to another cell whose membrane potential is

$V_{coupled}$, there is a current through the electrical coupling

$$i_{GJ} = \bar{g}_{GJ}\left(V_{coupled} - V\right), \tag{2.22}$$

where the gap junction coupling is placed at the somatic compartment. $\bar{g}_{GJ} = 0$ when the cell is not coupled to other cells. Finally, the membrane potential for the AII cell is described by

$$C\frac{dV}{dt} = \begin{cases} -\left(i_{Na} + i_A + i_M + i_{leak}\right) + i_{compart} & \text{for the IS,} \\ -\left(i_A + i_{leak}\right) + i_{compart} + i_{GJ} & \text{for the soma,} \\ -i_{leak} + i_{compart} & \text{for the cable,} \end{cases} \tag{2.23}$$

where C is the capacitance.

For the first set of simulations (Chapter 2.3.2, Figure 2.4), the model consisted of this three-compartmental AII in isolation, showing that a single AII is capable of generating tonic spiking and bursting. We adjusted the leak reversal potentials of the AII in order to reproduce the experimentally recorded membrane potentials for the wildtype and rd1 AII. We used the leak reversal potential of -10mV to put the AII in the tonic spiking regime, while using -50mV to put the AII in the bursting regime, capturing the rd1 AII being relatively hyperpolarized compared to the wildtype AII.

2.2.1.2. Single compartment model of ON cone bipolar cell. For the rest of the simulations (Chapter 2.3.3-2.3.5), an ON cone bipolar (ONCB) cell was electrically coupled to the three-compartmental AII cell. The ONCB cell was modeled as a passive single compartmental cell with surface area of 440 μm^2 and membrane resistivity 12,000 Ωcm^2.

The ONCB model was coupled to the "soma" compartment of the AII model, capturing its coupling to the AII arboreal dendrite, via a gap junction with a conductance of 750 pS. This is in the range of reported coupling strengths, which spans the range from 100 pS to 1,500 pS for type 5, 6, and 7 ONCB cells [**72**]. The leak reversal potentials for the AII and the ONCB in this coupled AII-ONCB model were adjusted to -65 mV and -35 mV, respectively, to reproduce the experimentally observed membrane potentials in rd1 retinas.

For the simulations in Chapter 2.3.6, the ONCB attached to the AII model was no longer modeled as a passive cell; instead, the ONCB is extended to include a FitzHugh-Nagumo type model, with

$$\frac{dV_{ONCB}}{dt} = \frac{1}{\tau} \cdot \frac{1}{\epsilon} F(V_{ONCB}, w) + \frac{\bar{g}_{GJ}}{C_{ONCB}}(V_{AII} - V_{ONCB}), \tag{2.24}$$

$$\frac{dw}{dt} = G(V_{ONCB}, w), \tag{2.25}$$

where

$$F(V_{ONCB}, w) = \frac{A(V_{ONCB} - vz_0)(V_{ONCB} - vz_1)(V_{ONCB} - vz_2)(V_{ONCB} - vz_4)}{(-V_{ONCB} + vz_3)} - w + \frac{Amp}{1 + e^{\frac{-(V_{ONCB} - Thr)}{Stp}}}$$

$$G(V_{ONCB}, w) = \frac{1}{\tau \cdot \tau_w \left(1 + \frac{\delta_\tau}{1 + e^{-\frac{V_{ONCB} - v_\tau}{v_\xi}}}\right)} (V_{ONCB} - \gamma w - v_0)$$

The parameters were chosen as following to replicate the slow Ca-induced oscillations observed in the experiments: $\epsilon = 0.000002$, $A = -0.01$, $vz_0 = -58$, $vz_1 = -48$, $vz_2 = -40$,

$vz_3 = -35$, $vz_4 = -61$, $\gamma = 30$, $v_0 = -58.5$, $Amp = 0.3$, $Thr = -56$, $Stp = 0.2$, $\tau = 8000$, $\tau_w = 2.5$, $\delta_\tau = -0.95$, $v_\tau = -55$, and $v_\xi = -1$. For this simulation, the surface area of the ONCB was reduced by 1/2.

2.2.2. Experimental methods

The intracellular recordings on AII amacrine (AII) cells were made from retinal slices; the recordings on retinal ganglion cells (RGCs) were from retinal whole-mount preparations. For extracellular recording of ganglion cell spiking, a ∼2 mm square of retinal tissue was mounted flat, ganglion cell-side down, onto a 60 channel multi-electrode array (MEA). The retinae were obtained from C3HeJ mice (*rd-1/rd-1*;RD1).

In all cases, during recordings, the tissues were super-fused with Ames-medium to which drugs were added as noted. Picrotoxin (100 μM), strychnine (0.5 μM), Dinitro-quinoxaline-2,3-dione (DNQX, 25 μM) and APV (50 μM) were added to block $GABA_A$ receptor-, glycine receptor-, AMPA/kainate receptor-, and NMDA receptor-mediated currents, respectively.

L-(+)-2-Amino-4-phosphonobutyric acid (L-AP4, 2-10 μM) was added to activate mGluR6 receptors on ON bipolar cells. Tetrodotoxin (TTX, 0.5 μM) was added to block voltage-gated Na channel-mediated currents, linopiridine hydrochloride (LP, 30 μM) was added to block M-type K currents, flupiritine maleate (flu, 10 μM) was added to potentiate M-type K currents, meclofenamic acid (MFA, 100 μM) was added to block gap junctions, and $CdCl_2$ (100 μM) and $NiCl_{2+}$ (50 μM) were added to block voltage-dependent Ca currents.

All the intracellular and extracellular recordings were made by the Singer laboratory. For detailed methods, see [**17**].

2.3. Results

2.3.1. MFA first slows down and then eliminates oscillations in rd1 retinas

It has been reported previously that the gap junction blocker meclofenamic acid (MFA) eliminates the oscillations in rd1 retina [**47, 68**]. Based on this observation, it has been suggested that oscillations are an emergent property of the gap-junction coupled network. More specifically, in a model network of AIIs with slightly heterogeneous properties, gap-junction coupling effectively could cause the AIIs to enter an oscillatory state even if the individual AIIs are not intrinsically oscillatory [**68**].

To characterize in more detail the effect of MFA on the AII network, membrane voltages of AII amacrine cells of rd1 mice were recorded in the Singer laboratory. The recordings confirmed spontaneous oscillatory activity in the AIIs of rd1 mice [**68, 77, 47, 60**], with frequencies in the range 5-15 Hz in agreement with previous studies [**68, 77, 47, 60**]. MFA was then applied, and the oscillation frequency and the membrane potential of rd1 AIIs (n=4) were measured. In these experiments, MFA application indeed was followed by elimination of the oscillations (Figure 2.1A). During the onset of the MFA effect, oscillations gradually decreased in frequency as the AIIs hyperpolarized. During MFA washout, oscillation frequency increased slowly until the original frequency was restored, and the mean AII membrane potential increased at the same time. Figure 2.1B shows that oscillation frequency varied directly with membrane potential.

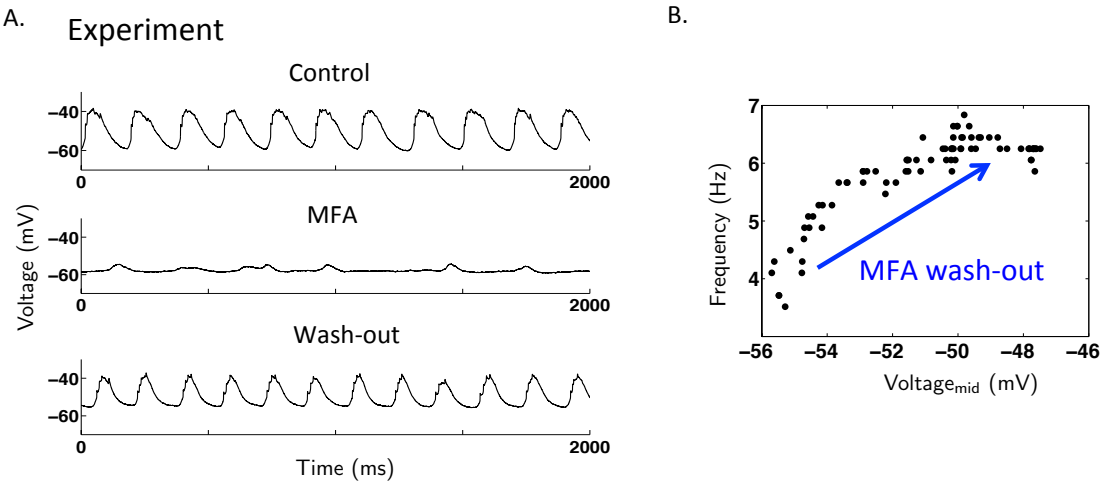

Figure 2.1. **MFA blocks oscillations following frequency decrease and hyperpolarization of AIIs.**
Experiment during MFA wash-in and wash-out on an rd1 AII. **A.** A representative recording of an rd1 AII shows that MFA eliminates the oscillations. The oscillation that was suppressed by MFA was restored with its frequency slowly increasing during the wash-out. **B.** The frequency averaged over each 5 s-long sweep is plotted as a function of the midpoint membrane potential of the AII during the MFA wash-out.

Motivated by these experimental results, we investigated whether such behavior during MFA application could be explained by the model put forward in [**68**]. This network model consists of two slightly heterogeneous AIIs and one ONCB. In agreement with [**68**], when we decreased the gap junction coupling strength, the oscillation amplitude decreased and eventually the oscillations stopped. However, the oscillation frequency increased during this process (Figure 2.2), which is inconsistent with the experimentally observed frequency decrease induced by MFA. This inconsistency motivated us to develop an alternative model to explain the rd1 oscillations.

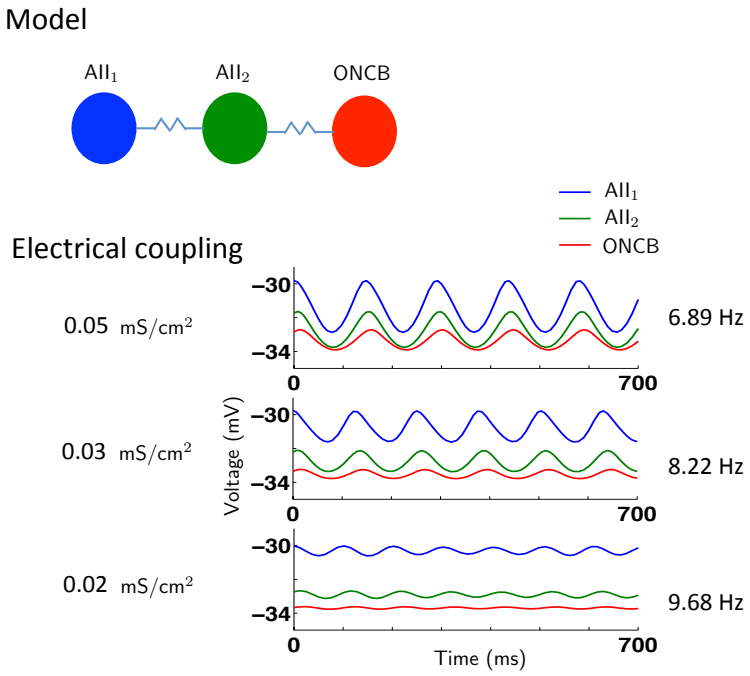

Figure 2.2. **A model based on gap junctions between heterogeneous AIIs does not explain the MFA-induced frequency decrease.** The model in Trenholm et al., 2012, which designates the gap-junction coupled network of heterogeneous AIIs as the key to the rd1 oscillations, does not explain the experimentally-observed frequency decrease under MFA application. The model consists of two slightly heterogeneous AII cells with Na, delayed rectifier K, and leak conductances, and an ONCB cell with a hyperpolarization-activated current and a leak current. All cells have a single compartment and are electrically coupled to each other. As the coupling strength decreases, mimicking the effect of MFA, the oscillation amplitude decreases, but the oscillation frequency increases in contrast to our experiments with MFA (Figure 2.1B). All the parameters used here are the same as in Trenholm et al., 2012 [**68**].

2.3.2. Rd1 oscillations resemble cable-filtered intrinsic bursting in AIIs

Upon closer inspection of the voltage wave form in the recordings from rd1 AIIs, small spikelets that arose during the depolarized phase of the oscillation were apparent (Figure

2.3A(i), inset). Such spikelets had been reported previously [**9**]. These oscillations were strikingly similar to those observed previously in AIIs of wildtype retina [**14**]. While without current injection wildtype AIIs spontaneously generated spikelets in a tonic fashion, upon hyperpolarization this tonic spiking became phasic (Figure 2.3A(ii)), leading to bursts of activity very similar in wave form and in frequency to the oscillations seen in AIIs of rd1 retina.

Since in the wildtype AIIs bursting arose only upon hyperpolarization, we compared the somatic voltages in the wildtype and rd1 AIIs in the absence of current injection. Because the wildtype AIIs were spontaneously spiking (within the range of -45 $\sim$ -40 mV, n=6, also [**14**]; Figure 2.3A(ii) before the hyperpolarizing current injection) and the rd1 AIIs were spontaneously oscillating (in the range of -65 $\sim$ -50 mV, n=6; Figure2.3A(i)), it is not possible to compare their resting potentials directly. Therefore, we compared the resting potentials of wildtype and rd1 AIIs under TTX. While there is notable variability between the cells, the resting potentials of the rd1 AIIs under TTX were significantly lower than those of the wildtype cells under TTX (-50.22 ± 2.1 mV, n=6 vs. -42.27 ± 4.9 mV, n=4; two-valued t-test $p < 0.015$), as shown in Figure 2.3 B.

Previous electrophysiology and computational modeling studies of wildtype AIIs showed that the small somatic spikelets are attenuated versions of full action potentials initiated in an electrically distal compartment, an aspect not captured by single-compartment models [**3**]. Moreover, hyperpolarization causes a transition to bursting involving a slow M-type K-conductance that periodically suppresses the spikes [**14**]. This bursting evokes small amplitude oscillations in the soma that include small spikelets during the depolarization phase, as in Figure 2.4B(ii). The similarities between the voltage waveforms in the rd1

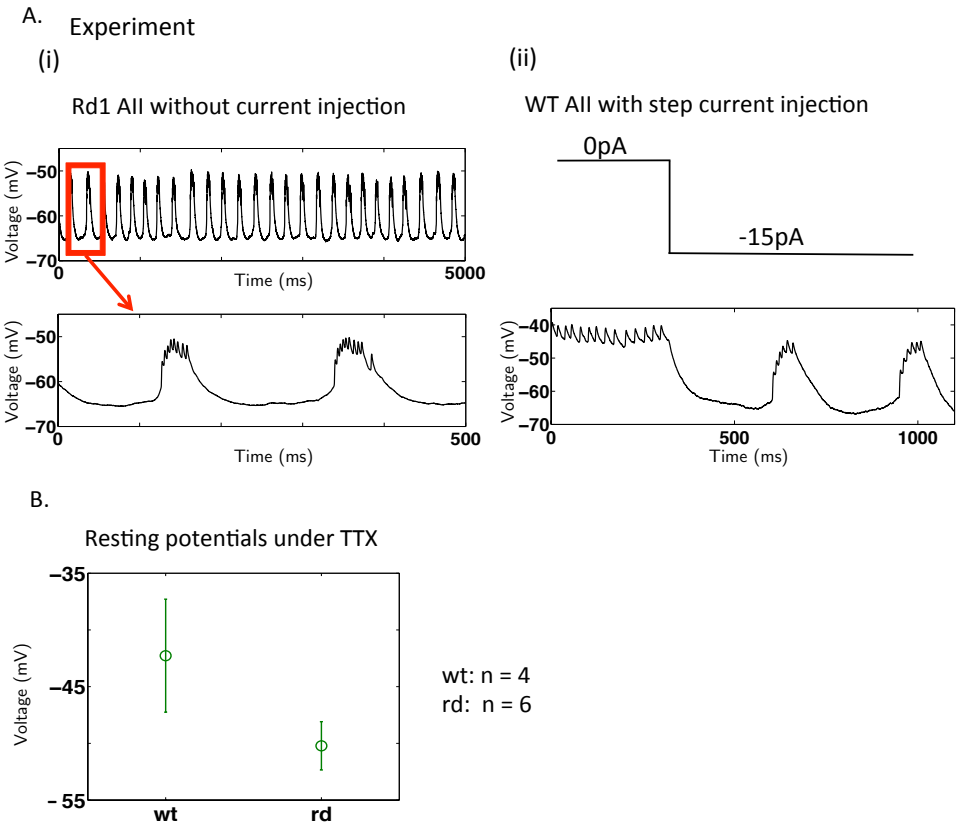

Figure 2.3. **Bursting in the hyperpolarized wt AII induces rd-like oscillations in the AII-cone bipolar network.**
A. Representative intracellular rd1 and wildtype AII recordings. (i) Oscillations in rd1 AII without hyperpolarizing current injection. (ii) The wt AII that exhibits spontaneous spikelets at rest (up to t=300ms), undergoes a transition to bursting when it is hyperpolarized (after t=300ms). **B.** Under TTX, the resting membrane potentials of wt AIIs (n=4) are more depolarized than those of rd1 AIIs (n=6).

AII and the hyperpolarized wt AII lead us to the hypothesis that oscillations in the rd1 retina are due to intrinsic bursting occurring in a distal initiation site of AII amacrine cells that have been hyperpolarized relative to wildtype conditions.

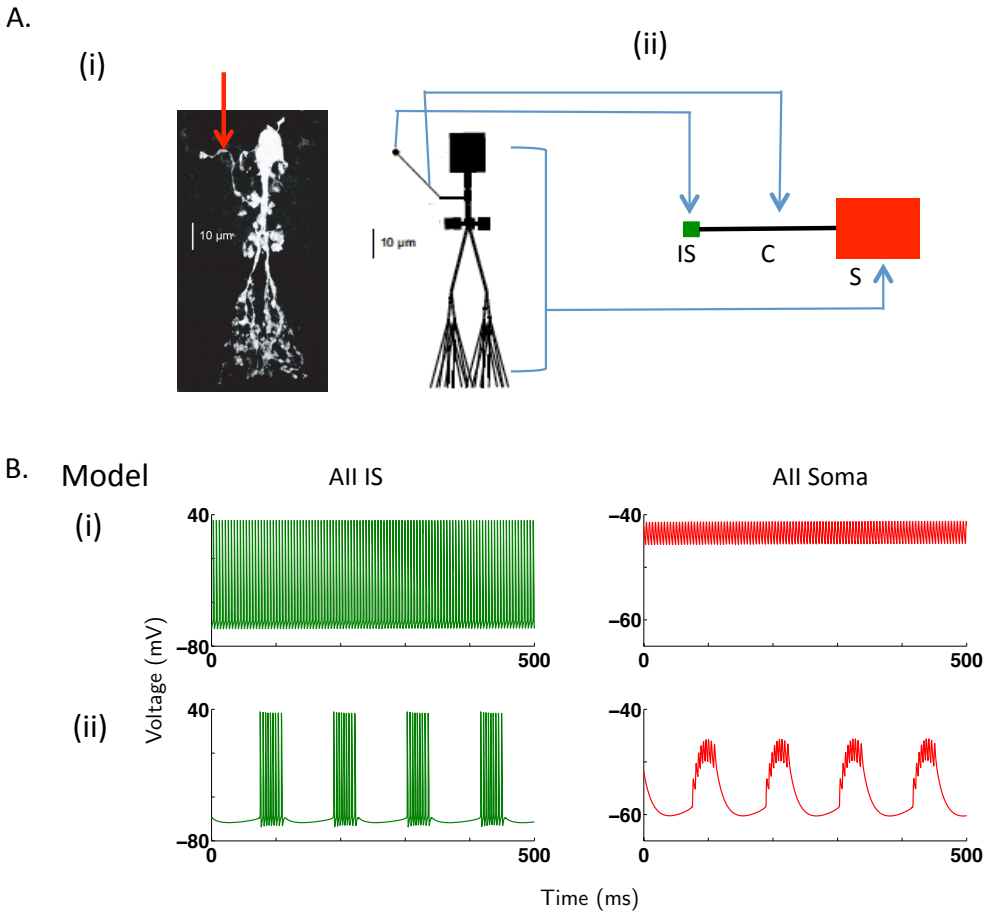

Figure 2.4. **Simulations showing tonic spiking and bursting of an AII.**
A. (i) A confocal image of an AII (left) and the morphologically detailed model (right). (ii) The reduced three-compartmental model of the AII consists of an "initiation site" (IS) and a "cable" (C) corresponding to the thin neurite branching from the primary dendrite of the AII (arrow in (i)), as well as a "soma" (S) which is taken to represent the rest of the AII (soma and dendrites). **B.** (i) Tonic spiking in the IS leads to small spikelets in the soma of the model wt AII. (ii) When the AII is hyperpolarized by lowering the leak reversal potential from -10mV to -50mV, to reproduce the experimentally observed membrane potentials of the wt and rd1 AII, the model AII shows spontaneous bursting.

2.3.3. The new rd1 AII model reproduces the MFA effects

A first test of this new model is whether it correctly reproduces the slowing down and elimination of bursting due to MFA application. Our hypothesis that the rd1 oscillations are generated by the intrinsic bursting of the AIIs is consistent with experiments employing MFA. MFA affects the AII-ONCB network beyond blocking the coupling between AIIs; it also reduces coupling between AIIs and ONCBs [**51**]. Since in the rd1 retina the ONCB cells are more depolarized (about -50mV, [**9**]) than the AIIs from our recordings (about -65 $\sim$ -50mV), blocking the electrical coupling between these should additionally hyperpolarize the AII. According to our model, such a further hyperpolarization can eliminate the bursting in individual AIIs, as shown in Figure 2.5A: as the model cell becomes hyperpolarized by current injection beyond the value that induces bursting, the frequency decreases and bursting eventually stops. Such behavior mimics the experimental results (Figure 2.1).

To test this interpretation further, we extended our model to include gap-junction coupling to a passive ONCB cell. We simulated the effect of MFA by reducing the coupling strength between the AII and the ONCB. As expected, weakening the coupling strength between the AII and the ONCB hyperpolarized the AII, which in turn decreased and then eliminated oscillations in AIIs, in agreement with the experiments (Figure 2.5B). If MFA stops oscillations by hyperpolarizing intrinsically oscillating AIIs, then, it should be possible to restore the oscillations by injecting depolarizing current into the AII following the application of MFA. Indeed, somatic current injections of $\sim$15-20pA restored bursting in AIIs in the experiments (Figure 2.6A) (n=4) and the model (Figure 2.6B). A similar result has been reported in [**68**].

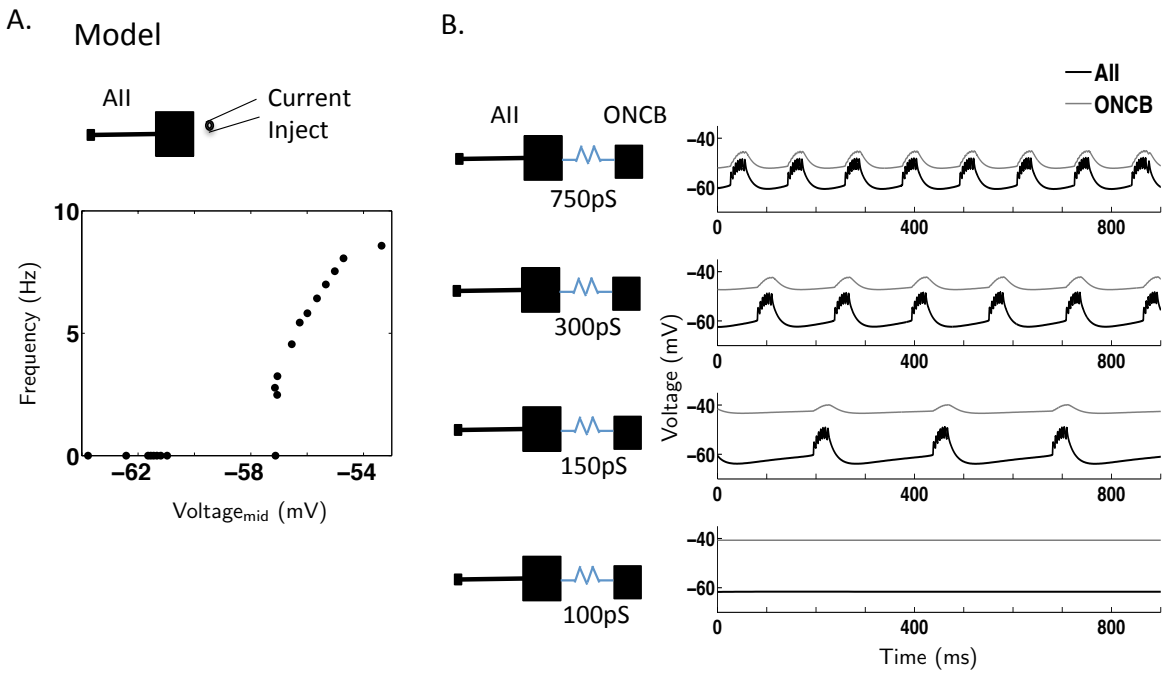

Figure 2.5. **Simulations support that MFA blocks oscillations via hyperpolarization of the AII.**
A. Simulation of hyperpolarizing current injection to the AII. The bursting frequency is shown as a function of the midpoint of the AII's membrane potential. **B.** Simulation of an AII coupled to an ONCB via a gap junction. As the coupling strength of the gap junction decreases, the bursting frequency also decreases. When the coupling strength is reduced to 100pS, bursting is eliminated.

2.3.4. M-current activator stops rd1 oscillations following frequency decrease

To investigate the hypothesized central role of the M-current in rd1 oscillations, the effect of the M-current activator flupirtine on rd1 retina was tested experimentally. Flupirtine is known to activate the M-type K current by shifting its activation to lower voltages [**75**]. During wash-in and wash-out of flupirtine, the membrane potential of rd1 AII cells was recorded (n=3).

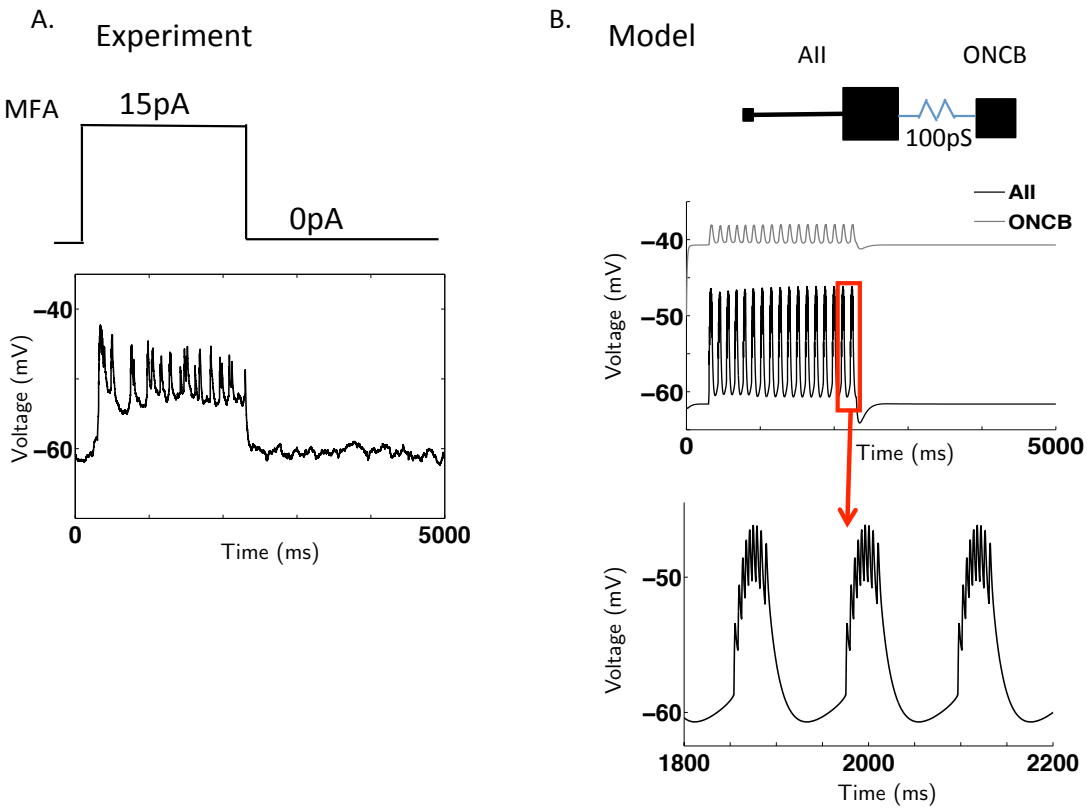

Figure 2.6. **Current injection following MFA application restores oscillations in rd1 AII.**
A. Experimental recording from an rd1 AII in which a depolarizing current injection of 15pA restored oscillations that had been silenced by MFA application. **B.** Simulation of a depolarizing current injection of 5pA to the model rd1 AII, with its gap junction coupling to the ONCB reduced to 100pS to mimic the effect of MFA. The oscillations are eliminated by a reduction in the gap junction coupling (Figure 2.5B), and are restored by the depolarizing current injection. The restored oscillations have the typical waveform (bottom figure).

During the wash-in of flupirtine, oscillations first decreased in frequency and then ceased (Figure 2.7A(i),(ii)). This pattern was reversed upon flupirtine wash out: silenced

AIIs first began to oscillate at low frequency, and then oscillation frequency rose. Concomitant with the change in frequency, the waveform of the oscillations evolved (Figure 2.7A(i)). To quantify the change in waveform, we measured the width of the bursts at a membrane potential that corresponded to 30% of the maximal oscillation amplitude in each sweep (1667 ms-long). As Figures 2.7A(iii) and (iv) show, the bursts became narrower during the wash-in of flupirtine (from 79.27 ± 4.45 ms to 44.9 ± 9.49 ms). To test the significance of the change, for this treatment and the following experiments, we performed a two-way ANOVA (here, 3 cells + 1 flupirtine application) on the natural logarithm of the burst duration. The effect due to flupirtine was found to be significant ($p < 10^{-3}$). Biophysically, with the left-shift of the activation curve of the M-current fewer spikes are required to generate an outward current sufficient to shut off the spiking.

We also simulated the effect of flupirtine in our model AII by shifting the half-activation voltage ($V_{1/2}$) of the M-type K current to lower voltages. Consistent with the experiments, this manipulation decreased bursting frequency and then silenced the cell (Figure 2.7B). While the frequency generally decreased as $V_{1/2}$ of the M-current became more negative, there were also discrete jumps around $V_{1/2} = -42$ mV and $V_{1/2} = -45$ mV (Figure 2.7B(ii)). These jumps occurred due to a reduction in the number of spikes per burst. In the experiments the individual bursts were too variable to allow the identification of such details (cf. Figure 2.3A(i)). As in the experiment, however, the burst width decreased (Figure 2.7B(i)).

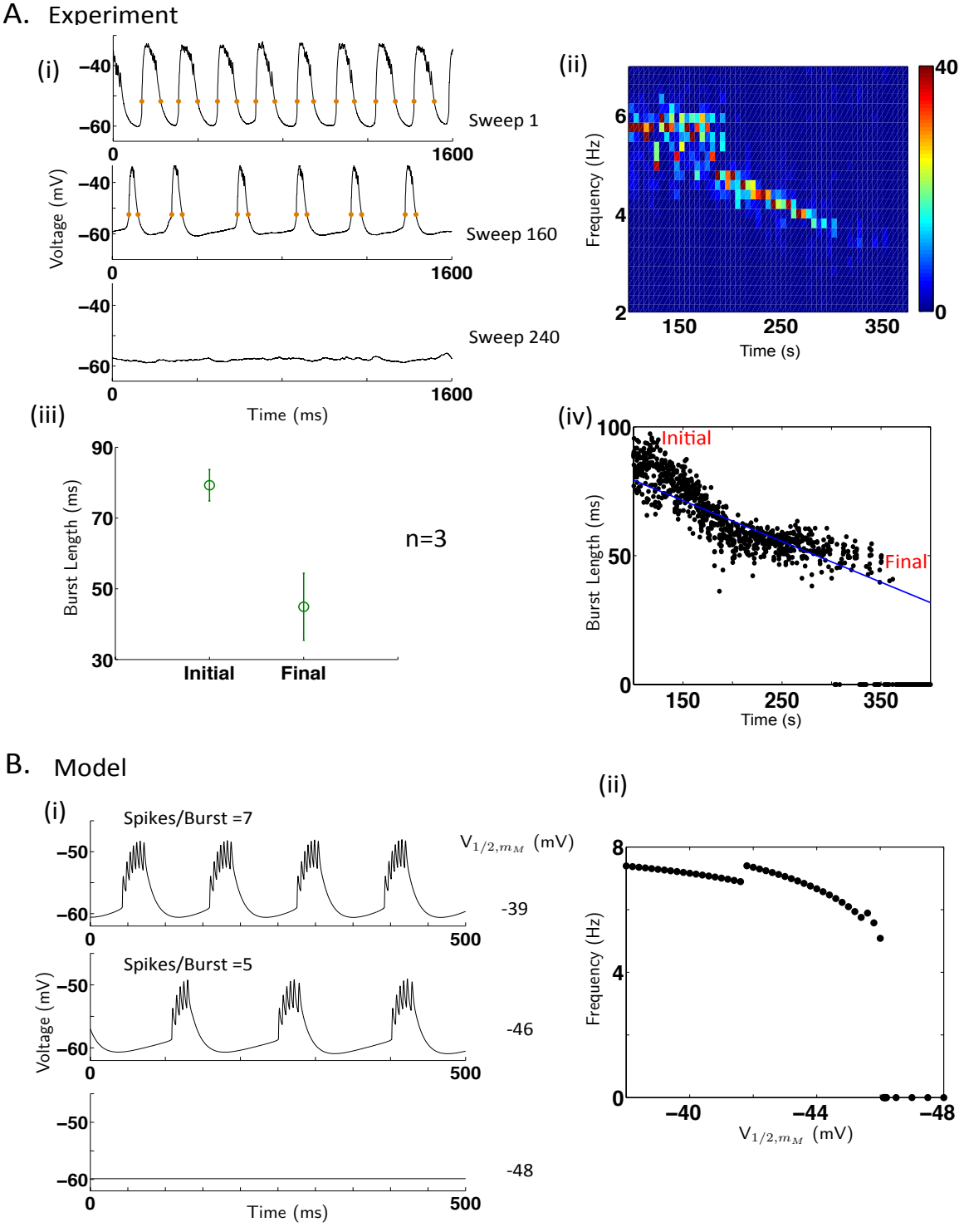
A. Experiment
(i)
−40
−60
Sweep 1
0
1600
Voltage (mV)
−40
−60
Sweep 160
0
1600
−40
−60
Sweep 240
0
1600
Time (ms)
(ii)
Frequency (Hz)
6
4
2
150
250
350
Time (s)
40
0
(iii)
Burst Length (ms)
90
70
50
30
n=3
Initial
Final
(iv)
Burst Length (ms)
100
50
0
Initial
Final
150
250
350
Time (s)
B. Model
(i)
Spikes/Burst =7
$V_{1/2,m_M}$ (mV)
−50
−60
-39
0
500
Spikes/Burst =5
Voltage (mV)
−50
−60
-46
0
500
−50
−60
-48
0
500
Time (ms)
(ii)
Frequency (Hz)
8
4
0
−40
−44
−48
$V_{1/2,m_M}$ (mV)

2.3.5. M-current blocker disrupts the ∼10Hz oscillations and induces slow Ca channel-mediated oscillations

To determine how antagonizing the M-type K channel affects the rd1 oscillations, linopirdine dihydrochloride (LP) was used. Blocking the M-current reduced the burst frequency (Figure 2.8A(i),(ii); n=5). The burst duration, however, increased from 87.36 ± 41.09 ms to 175.04 ± 34.69 ms; this is opposite to the effect of flupirtine on the burst duration. Despite its marked variation across the recorded cells, the increase was highly significant ($p < 10^{-3}$) (Figure 2.8A(iii),(iv)). In agreement with this observation, the computational model also generated lower burst frequencies and longer burst durations when the maximal M-conductance was reduced (Figure 2.8B). This was expected, since the M-current has been identified as being responsible for terminating spiking [**14**].

Figure 2.7 *(preceding page).* **Opening M-current reduces frequency and burst length, and stops oscillations.**
A. Experiment during flupirtine wash-in on an rd1 AII. (i) Representative traces of the AII membrane potential during flupirtine wash-in. (ii) The spectrogram of the recording in (i) shows that the frequency decreased under flupirtine application, eventually resulting in termination of the oscillations. (iii) The burst length at the end of the flupirtine wash-in (final) is significantly smaller than at the beginning (initial) ($n = 3$, $p < 10^{-3}$). (iv) Burst length during the flupirtine wash-in of a representative recording. The length was measured at 30% of the maximal oscillation amplitude for each 1667ms-long sweep (orange dots in (i)). The red "Initial" and "Final" indicate where the initial and final burst lengths were measured.**B.** Simulation mimicking flupirtine application by moving the half-activation voltage $V_{1/2}$ of the M-conductance leftward. (i) Representative membrane potential traces for the model AII. Along with the frequency decrease, the number of spikes per burst decreases as well, resulting in burst length decrease. (ii) In the model the burst frequency decreases as the half-activation voltage $V_{1/2}$ of the M-conductance is reduced. The discrete jumps correspond to reduction in the number of spikes per burst. Eventually the AII becomes quiescent.

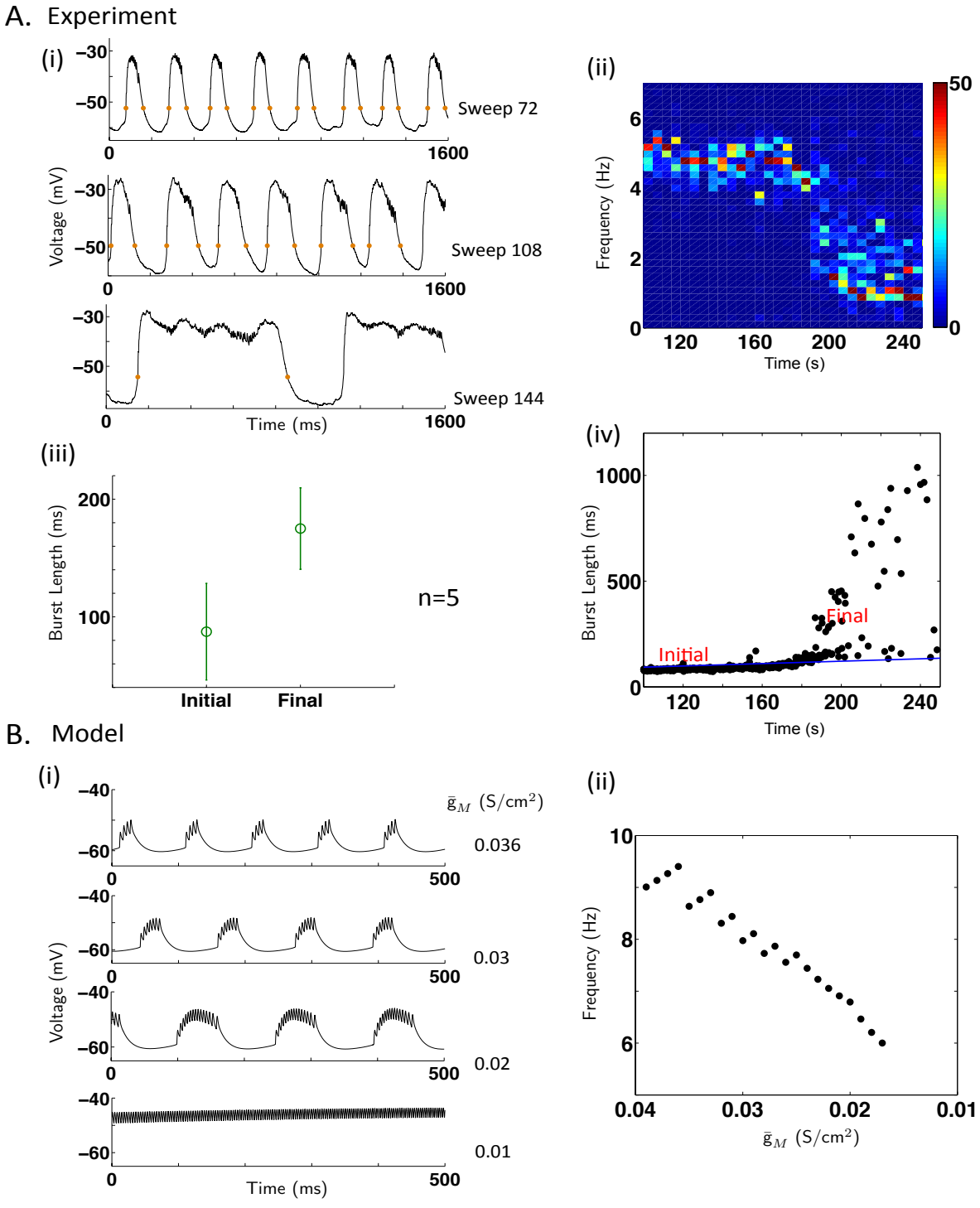
A. Experiment
(i)
−30
−50
Sweep 72
0
1600
Voltage (mV)
−30
−50
Sweep 108
0
1600
−30
−50
Sweep 144
0
Time (ms)
1600
(ii)
Frequency (Hz)
6
4
2
0
120
160
200
240
Time (s)
50
0
(iii)
Burst Length (ms)
200
100
n=5
Initial
Final
(iv)
Burst Length (ms)
1000
500
0
Final
Initial
120
160
200
240
Time (s)
B. Model
(i)
−40
−60
$\bar{g}_M$ (S/cm^2)
0.036
0
500
Voltage (mV)
−40
−60
0.03
0
500
−40
−60
0.02
0
500
−40
−60
0.01
0
Time (ms)
500
(ii)
Frequency (Hz)
10
8
6
0.04
0.03
0.02
0.01
$\bar{g}_M$ (S/cm^2)

In the model, decreasing the M-current caused the burst duration to increase without bounds and eventually to elicit tonic spiking. In the experiments, however, LP did not eliminate all oscillations and it did not induce tonic spiking. Instead, when the burst duration increased beyond ∼200 ms, a transition to a different type of low-frequency (∼1 Hz) oscillation occurred (Figure 2.8A(i) bottom panel, Figure 2.9B). Riding atop these slow oscillations were faster, though irregular, 5-10 Hz bursts of spikes. These bursts were reminiscent of the characteristic rd1 oscillations that were observed in the absence of LP. This phenomenon was also observed when ONCBs first were hyperpolarized by application of L-AP4, which on its own does not block oscillations in the rd1 retina [**9**] (n = 6; data not shown). Because of this transition to a qualitatively different type of

---

Figure 2.8 *(preceding page).* **Blocking M-current reduces frequency and increases burst length.**
A. Experiment during LP wash-in on an rd1 AII. (i) Representative traces of the AII membrane potential during LP wash-in. The trace corresponding to the ∼1Hz frequency (bottom panel) had a characteristic waveform consisting of overshoots and a plateau that differed from the waveform of the typical rd1 oscillations. (ii) The spectrogram of the recording in (i) shows that the frequency decreased under LP application, eventually reaching a very low frequency of ∼1Hz. (iii) The initial and the final burst lengths during LP wash-in show a significant increase ($n = 5$, $p < 10^{-3}$). The final burst lengths were measured right before the transition to the ∼1Hz oscillations. (iv) The burst length increase during the LP wash-in of a representative recording. The length was measured at 30% of the maximal oscillation amplitude for each 1667ms-long sweep (orange dots in (i)). The red "Initial" and "Final" indicate where the initial and final burst lengths were measured. **B.** Simulation mimicking LP application by reducing the M-current maximal conductance $\bar{g}_M$. (i) Representative membrane potential traces for the model AII. While the burst frequency decreases, the number of spikes per burst increases, resulting in burst length increase. (ii) In the model the burst frequency decreases as the M-conductance decreases. The discrete jumps correspond to increase in the number of spikes per burst. Below $g_M = 0.015$ S/cm^2 the AII exhibits tonic spiking.

oscillation the measurement of the increase in the burst duration due to LP depended on the identification of the transition time. We used the sudden increase in the variability of the duration as a criterion for that transition.

The low-frequency oscillation resembled both in frequency and shape the slow, Ca channel-mediated oscillations that have been observed in ONCB cells of rat, mouse, and goldfish retina when inhibition was blocked [**40, 77, 78**]. In order to test whether the slow oscillations were indeed Ca channel–mediated, cadmium (Cd^{2+}) and nickel (Ni^{2+}), two non-selective voltage-gated Ca^{2+} channel blockers, were applied after the slow oscillations induced by LP had been established (in the presence of L-AP4, n=4). The characteristic shape and frequency of the slow oscillations induced by LP were disrupted by Ni^{2+} and Cd^{2+}, supporting our hypothesis that the slow oscillations that appear under LP-application require Ca channels and therefore arise from a mechanism that differs from that underlying the $\sim$10Hz oscillations (Figure 2.9).

Thus, either blocking or potentiating an M-type K conductance eliminates the characteristic 5 -10 Hz oscillations in rd1 AIIs (Figure 2.7, 2.8). The observed changes in oscillation frequency and burst duration are predicted by our model of a single AII. This suggests that the slow M-type K current plays the same key role in generating the rd1 oscillations as it does in generating bursting in wt AIIs.

Note that the model investigated in [**68**] does not include an M-current and therefore does not allow any predictions pertaining to these experiments.

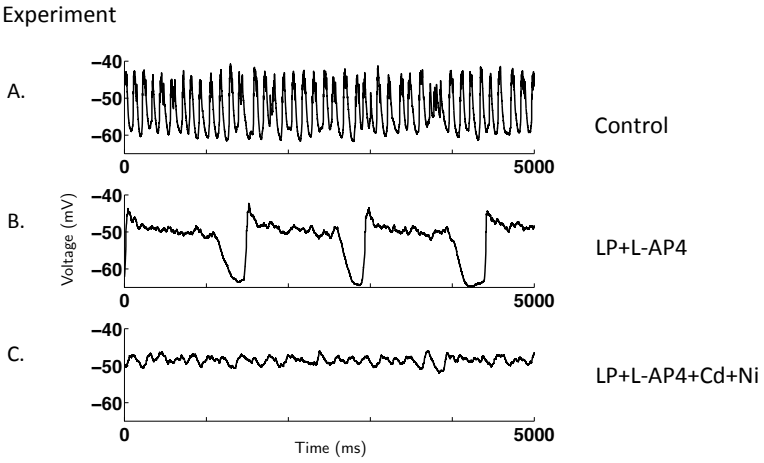

Figure 2.9. **Blocking Ca^{2+} channels disrupts the slow-frequency oscillations.**
A representative recording of an rd1 AII under LP and Ca^{2+}-blockers. The characteristic rd1 oscillations, which were unaffected by L-AP4 (**A**), were disrupted by LP and replaced by slow-frequency oscillations (**B**). The slow-frequency oscillations were eliminated by Ni^{2+} and Cd^{2+} (**C**).

2.3.6. Phenomenological model of the slow Ca channel-dependent oscillations

We found that application of the M-current antagonist LP reduced oscillation frequency and lengthened the burst duration, consistent with our model (Figure 2.8). LP, however, also induced slow (∼1 Hz) oscillations in AIIs that appeared to involve Ca channels (Figure 2.9). The frequency and waveforms of bursts underlying these slow oscillations resembled Ca channel-dependent regenerative activity observed previously in isolated ONCBs [**40**] and in whole retinas when inhibition was blocked [**77**]. We speculate that the enhanced burst duration in the presence of LP may allow activity in AIIs to trigger such regenerative events in ON cone bipolar cells; in turn, the regenerative events in ON cone bipolar cells modulate the AII voltage.

To illustrate the feasibility of such a scenario, we extended our passive ON cone bipolar cell model to include a simple model of FitzHugh-Nagumo type [**25**] to allow for regenerative events; active ON cone bipolar cells were coupled to model AIIs. The single compartment ONCB, which is coupled to the three-compartment AII model with the coupling strength $\bar{g}_{GJ} = 500$pS, is modeled by

$$\frac{dV_{ONCB}}{dt} = \frac{1}{\tau} \cdot \frac{1}{\epsilon} F(V_{ONCB}, w) + \frac{\bar{g}_{GJ}}{C_{ONCB}}(V_{AII} - V_{ONCB}), \tag{2.26}$$

$$\frac{dw}{dt} = G(V_{ONCB}, w), \tag{2.27}$$

The details of the model can be found in the Methods 2.2.1.2.

In this simulation, decreasing the maximal M-type K conductance in a sigmoidal fashion to mimic LP application generated a sudden transition from short bursts to much longer depolarizing events upon which spiking was superimposed (Figure 2.10B). This transition can be explained by analyzing the nullclines of the dynamic variables in the model ONCB. In Figure 2.10A, the black line represents the nullcline of w, which depends only on the V_{ONCB} and does not change much during bursting. The blue and red lines are the V_{ONCB}-nullclines when the membrane potential of the coupled AII is at -50 mV (around the maximal voltage during AII bursting) and -60 mV (around the minimal voltage during AII bursting), respectively. Therefore, when the AII is bursting, the V_{ONCB}-nullcline moves between the blue and red nullclines in Figure 2.10A. Because ϵ is small, the trajectory moves faster in the direction of V_{ONCB} than in the direction of w.

The V_{ONCB} is around -59 to -58 mV and the w stays around 0.004–0.013 before the system undergoes a transition to the slow, ONCB-driven oscillations. When $\bar{g}_M$ is large

and the burst duration is short, the V_{ONCB}-nullcline moves between the blue and red nullclines rapidly. In this case, the trajectory is trapped in between the blue and red nullclines and thus attracted to the leftmost fixed point where the w-nullcline crosses the V_{ONCB}-nullcline. More specifically, the attracting fixed point moves up and down as the V_{ONCB}-nullcline moves between the blue and red nullclines. When the V_{ONCB}-nullcline moves up quickly, the system cannot follow the fixed point as fast and effectively the previous fixed point location becomes an initial condition under the new conditions. When the burst duration is short, the nullcline moves down to the red nullcline fast enough so that the trajectory does not move far enough to the right before the fixed point is moved down again.

As $\bar{g}_M$ decreases, the burst duration increases as indicated by the number of spikes per burst in Figure 2.10B. As the burst duration increases, the V_{ONCB}-nullcline moves between the blue and red nullclines more slowly. Eventually, the change in the V_{ONCB}-nullcline becomes slow enough so that the trajectory is no longer trapped. The attracting fixed point formed by the intersection of the V_{ONCB} -nullcline and the w-nullcline moves up when the V_{ONCB}-nullcline moves up to the blue nullcline. Since the V_{ONCB}-nullcline stays near the blue nullcline for a while as the burst duration is longer and the horizontal motion is faster than the vertical motion due to small ϵ, the trajectory moves rapidly in the direction of increasing V_{ONCB} until it reaches the V_{ONCB}- nullcline around -35 mV, initiating the slow oscillations. In other words, the prolonged burt duration allows the system to make it far enough to the right before the fixed point is moved down again, and generates the low-frequency oscillations similar to the Ca-dependent oscillations observed in the experiments.

We did not, however, assess whether this model captured all aspects of the experimentally observed transition to the slow oscillations induced by LP; while this is an interesting question, we considered it to be beyond the scope of the current work.

2.3.7. Rd1 oscillations in retinal ganglion cells are driven by the intrinsic AII oscillations

In rd1 retina, the 5-15Hz oscillations are also observed in ganglion cells, the retinal output cells that receive signals from AIIs either directly (OFF ganglion cells) or indirectly via ON/OFF cone bipolar cells (to ON and OFF ganglion cells, respectively). The ganglion cells then transmit the retinal signals to the brain. In previous studies, it has been shown that the oscillatory activities in RGCs were eliminated in the presence of synaptic blockers, indicating cells upstream to RCGs as the generator of the oscillations [**46, 9, 47, 60, 76, 77**]. Furthermore, in a recent study [**45**], it was observed that the rhythmic activities in RGCs in pairs of ON/ON or OFF/OFF ganglion cells were in phase, while those in pairs of ON/OFF ganglion cells were out of phase. These results are consistent with the AIIs being the source of the oscillations in RGCs. Having found evidence to support the hypothesis that the rd1 oscillations in AIIs are intrinsically generated by their M-type K conductance, we next investigated whether these AII oscillations are indeed the origin of the RGC oscillations. Therefore, the effects of LP and flupirtine on the oscillations in RGCs in the rd1 retina were tested. The oscillations were measured with intracellular recordings of single alpha ganglion cells in the rd1 whole mount retina, as well as extracellular recordings. For the extracellular recordings, both single and multi-units were measured via multielectrode arrays (MEA).

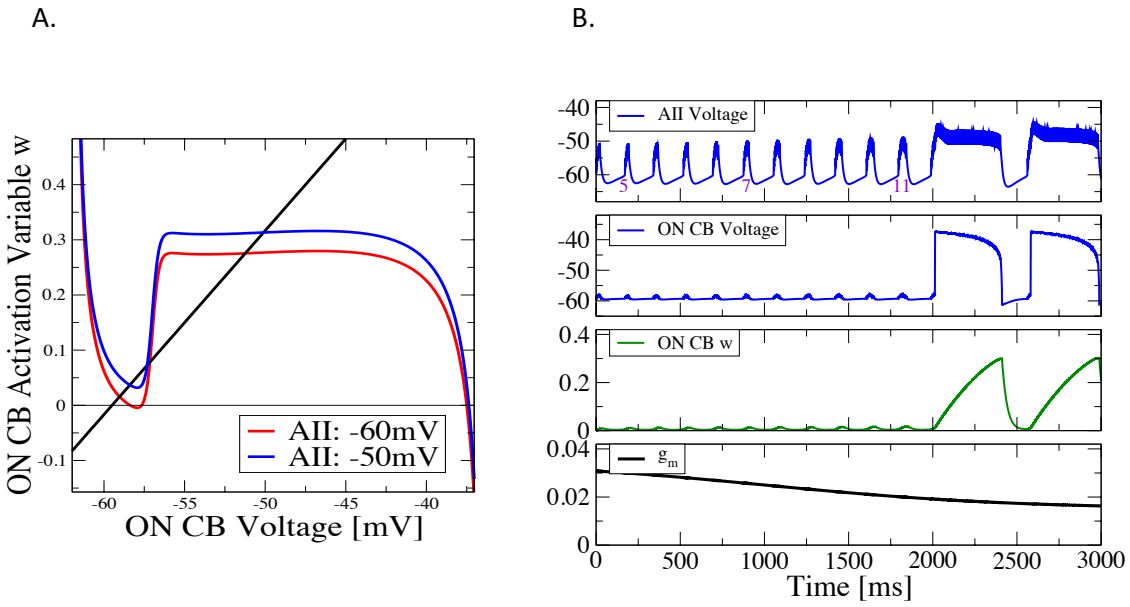

Figure 2.10. **FitzHugh-Nagumo type model of Ca^{2+}-mediated slow oscillations in an ONCB coupled to an AII.**
In this simulation, $\bar{g}_M$ decreases in a sigmoidal fashion mimicking LP application. The burst duration increases, and when it reaches a critical value, the wave form makes a transition from the characteristic rd1 oscillations to qualitatively different slow oscillations. **A**. Nullclines of V_{ONCB} (blue and red) and w (black). When $\bar{g}_M$ is large, the burst duration is short, and the V_{ONCB} nullcline moves between the red and the blue nullclines which correspond to the V_{ONCB} nullclines at the maximum and minimum voltages during bursting. As the V_{ONCB} nullcline changes fast when the burst duration is short, the model gets attracted to the fixed point. However, as $\bar{g}_M$ decreases, the burst duration increases and thus the V_{ONCB} nullcline moves between the blue and the red nullclines slowly. Then the variables jump to the branch at a higher ONCB voltage and therefore generate the large amplitude relaxation oscillation. **B**. AII voltage, ONCB voltage and w variable as $\bar{g}_M$ decreases in a sigmoidal fashion (bottom panel). The number of spikes per burst increases as indicated in the top panel.

In the intracellular recordings, both flupirtine and LP disrupted the oscillations in RGC membrane potentials. Moreover, the changes in frequency and burst duration were consistent with those in AII oscillations; under flupirtine, the elimination of the oscillations followed a decrease in both frequency and burst duration, while LP decreased the bursting frequency and increased the burst duration before eliminating the rd1 oscillations. Representative traces of ganglion cell membrane potentials along with their frequency and burst duration changes under flupirtine and LP are shown in Figures 2.11A and B (i),(ii),(iv) respectively. Figures 2.11A(iii) and B(iii) show the collective data of burst duration changes under flupirtine and LP. In retinas treated with LP (n=4), the width of ganglion cell bursting increased (from 38.52 ± 27.78 ms to 305.25 ± 108.45 ms, $p < 10^{-3}$). In 3 out of 4 cells under flupirtine, the burst widths decreased (from 51.68 ± 12.4 ms to 17.37 ± 8.37 ms, $p < 10^{-3}$). In one case, application of flupirtine was followed by almost instant elimination of the oscillations, so it was not possible to observe slow changes in the burst duration. In addition, in 3 out of 4 cells treated with flupirtine, the bursting frequency became irregular before the cells became quiescent. However, in all cases, the spikes became less frequent after flupirtine application.

In the extracellular electrode recordings, the oscillations present in each single unit as well as in the multi-unit activity were studied. Both single and multi-unit activities agreed with the changes in AII oscillations under LP application. A representative single unit activity is shown in Figure 2.12A. It is apparent that the oscillations under LP are slower than those in L-AP4 and wash out conditions. Similarly, the interspike intervals show a nonzero peak at a much higher value (810 ms) under LP than under L-AP4 or wash out. Figure 2.12B shows the comprehensive bursting statistics of single units. Under L-AP4

(n=61), the single unit burst lengths had a median value of 49 ms with an interquartile range (IQR) of 45-59 ms. The frequency of these oscillations had a median 6.2 Hz with IQR 4.8-6.7 Hz. When LP was applied, the burst lengths of the single units (n=18) increased to 64 ms and their IQR ranged from 40 to 120 ms. The frequency of these oscillations decreased to a median of 1.37 Hz with an IQR of 1.08-1.6 Hz, consistent with what was observed from AIIs under LP. Then, for the wash out condition, the oscillation frequencies of the single units (n=34) increased back to near the values found for the initial L-AP4 condition, and the mean burst length decreased to 51 ms, with IQR = 39-67ms.

We also analyzed the effects of LP on multi-unit activity (MUA) using data from the Singer lab. The spectograms of the MUA in Figure 2.13A show that LP application slowed the MUA oscillations. Based on the MUA, oscillating channels under the L-AP4 condition (n = 52) had a median oscillation frequency of 7.5 Hz and an IQR of 4.8-9.6 Hz. For the LP condition (n=70), the oscillating channels had a median frequency of 1.75 Hz and IQR of 1.2-4.8 Hz. Then for the wash out condition (n=66), we observed that the oscillation frequencies increased back towards their initial values (Figure 2.13B).

The extracellular recordings were also made under flupirtine (2 experiments), and either complete elimination of the oscillations or a decreased bursting frequency was observed. However, extracellular recording summary statistics are not reported here for the bursting activity of RGCs under flupirtine, because the Singer lab did not isolate a statistically significant number of single units for this condition (n=7).

In conclusion, intracellular recordings, single unit extracellular recordings, and multi-unit extracellular recordings all show elimination of the oscillatory activities in RGCs

under LP and flupirtine. Moreover, the changes in burst frequency and burst duration in RGCs agree with those in AIIs, providing strong evidence that the oscillations in RGCs indeed come from the upstream AII cells in the rd1 retina.

2.4. Discussion

As described in the results, we combined computational model with experiments in the Singer lab to test the hypothesis that oscillations of AIIs in the rd1 retina are intrinsic and the result of interactions between fast, depolarizing Na and slow, hyperpolarizing, M-type K conductances. In this scenario, the oscillations arise as the result of spontaneous bursting in a distal compartment generated because rd1 AIIs are hyperpolarized relative to wt AIIs. We analyzed a compartmental model of the AII [**14**] to predict the expected electrophysiological responses of AIIs to pharmacological manipulation of M-type K currents, and performed these experiments. The combined computational and experimental results are fully consistent with our hypothesis. Additionally, single-cell and multi-electrode array recordings from ganglion cells demonstrated that altered AII activity was propagated unchanged to ganglion cells. Our conclusion is that the oscillatory output of ganglion cells in the rd1 retina reflects the intrinsic properties of AII amacrine cells.

2.4.1. Clinical implications

A recent study demonstrates that MFA blocks the characteristic oscillatory activity of retinas of rd10 mice, which have a less severe retinal-degeneration phenotype than rd1 mice, and improves signal transmission from surviving photoreceptors to ganglion cells

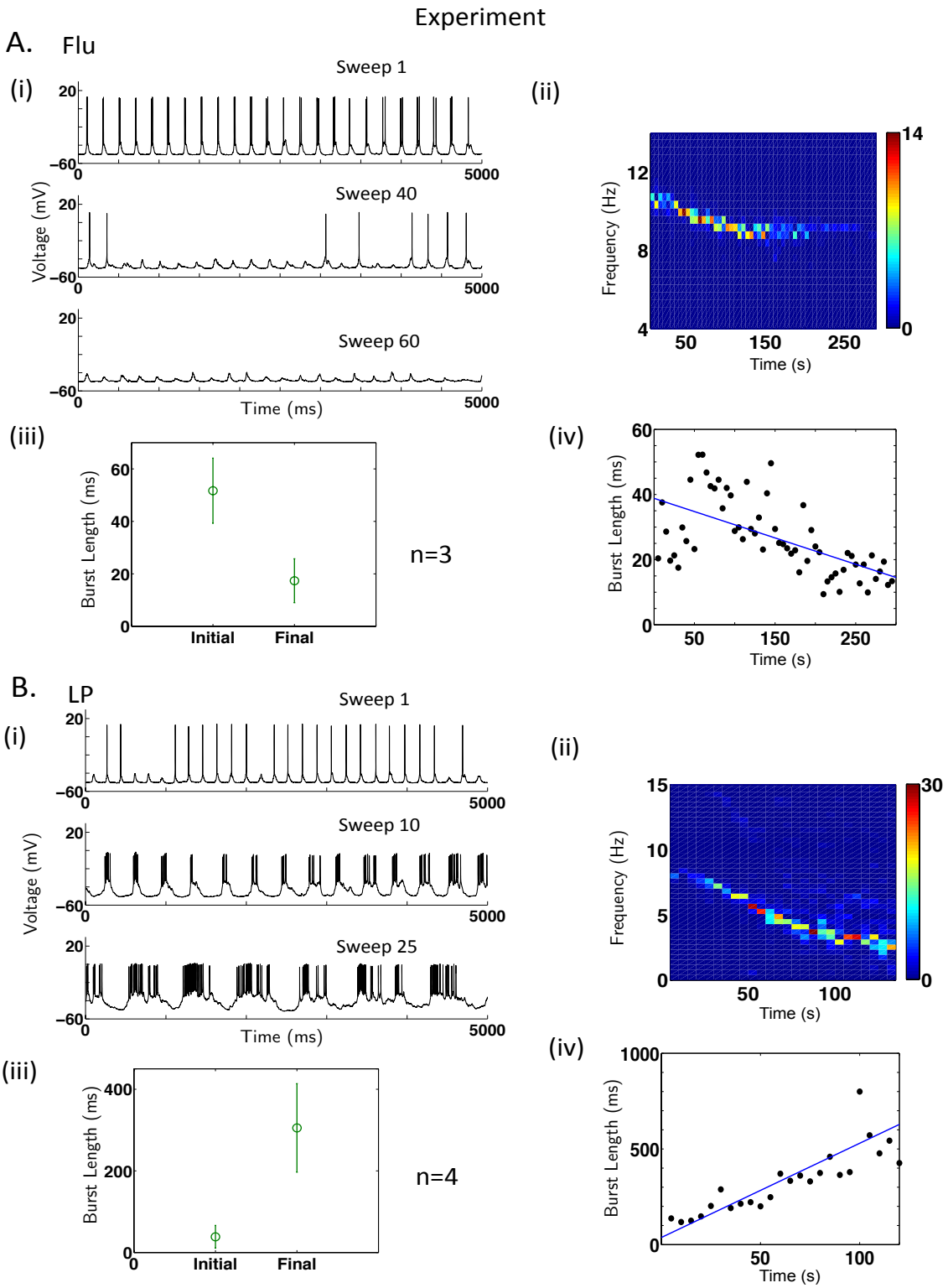
Experiment
A.
Flu
(i)
Sweep 1
Sweep 40
Sweep 60
Voltage (mV)
Time (ms)
(ii)
Frequency (Hz)
Time (s)
(iii)
Burst Length (ms)
Initial
Final
n=3
(iv)
Burst Length (ms)
Time (s)
B.
LP
(i)
Sweep 1
Sweep 10
Sweep 25
Voltage (mV)
Time (ms)
(ii)
Frequency (Hz)
Time (s)
(iii)
Burst Length (ms)
Initial
Final
n=4
(iv)
Burst Length (ms)
Time (s)

[**67**]. This finding is difficult to interpret, however, since gap junctions mediate interactions among many different classes of retinal neurons. Thus, blocking all gap junctions may not be the most advantageous therapeutic intervention.

Our study indicates that MFA application eliminates oscillations not by uncoupling the AII network but by hyperpolarizing intrinsically active AIIs. As a result manipulating the resting membrane potential of AIIs in some other manner might be an effective and benign way to restore signaling in a deteriorating retina. Introducing light sensitivity into bipolar cells [**37**] or stimulating them with retinal prostheses [**62**] are possibilities that may be sufficient to reduce hyperpolarization of AIIs and keep them from bursting.

2.4.2. Role of gap junctions among rd1 AIIs

We found that the oscillations in AIIs that are eliminated by MFA application can be rescued by depolarizing current injections. This indicates that the gap junction coupling among AIIs is not essential for the generation of rd1 oscillations, but that the gap junctions between AII and ONCB play a role by affecting the AII resting potential. It is likely,

---

Figure 2.11 *(preceding page).* **The intracellularly recorded rd1 oscillations in retinal ganglion cells change similarly to those in AIIs under M-current activator and blocker.**
A. The rd1 oscillations in RGCs were disrupted in the presence of flupirtine. (i) A representative RGC membrane potential under flupirtine. Flupirtine decreased oscillation frequency (ii) and decreased burst duration (iv). (iii) The initial and the final burst lengths during flupirtine wash-in show a significant decrease (n=3, $p < 10^{-3}$). **B**. The rd1 oscillations in RGCs were disrupted in the presence of LP. (i) A representative RGC membrane potential under LP. LP induced a decrease in oscillation frequency (ii) and increase in burst duration (iv). The burst durations were averaged for each 5s-long sweep. (iii) The initial and the final burst lengths during LP wash-in show a significant increase (n=4, $p < 10^{-3}$).

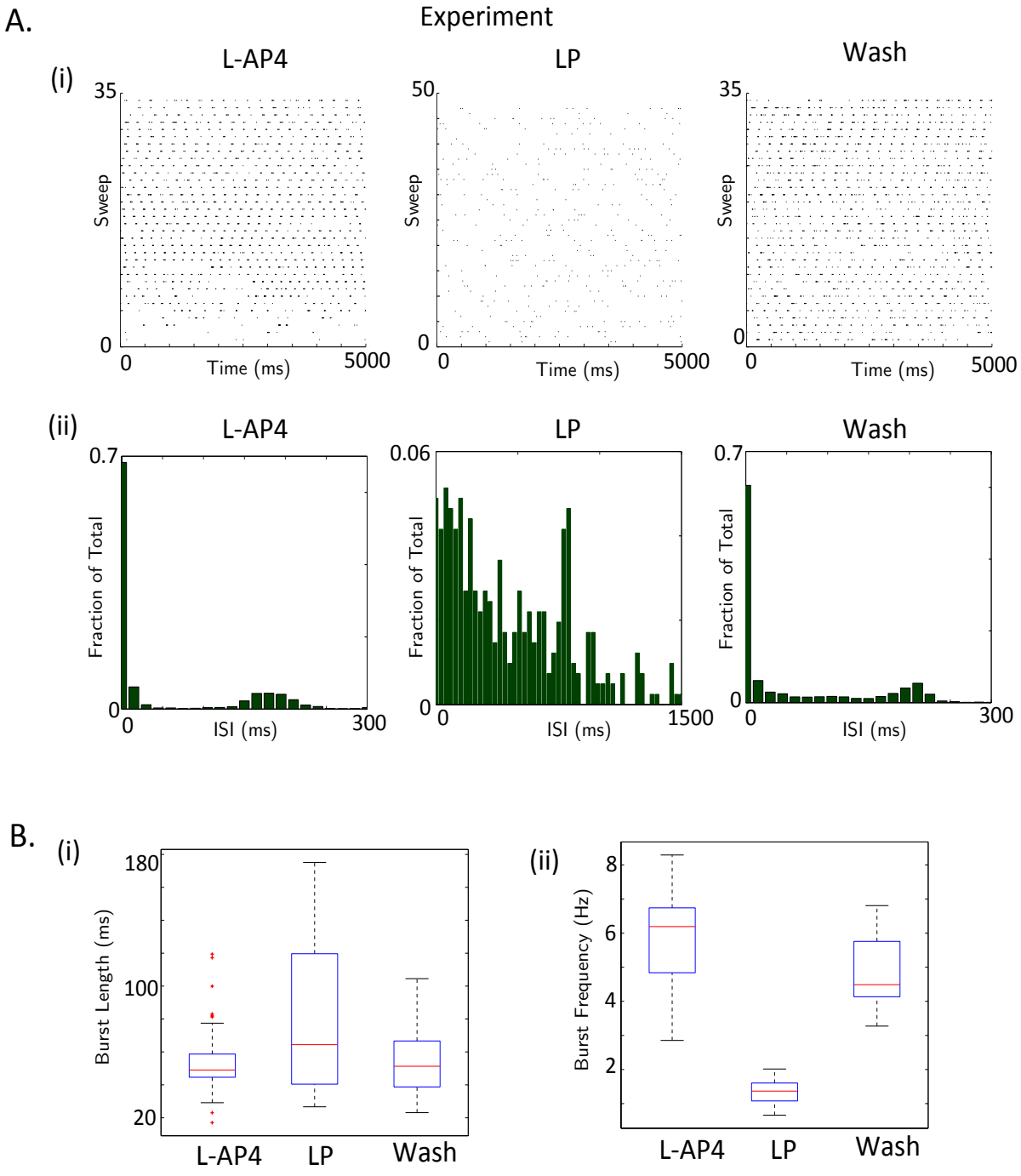
A.
Experiment
(i)
L-AP4
LP
Wash
35
50
35
Sweep
0
Time (ms)
5000
(ii)
0.7
0.06
Fraction of Total
ISI (ms)
300
1500
B.
(i)
180
100
20
Burst Length (ms)
(ii)
8
6
4
2
Burst Frequency (Hz)

however, that the gap junction coupling among AIIs synchronizes the oscillations and allows them to propagate through the network.

For example, in a gap junction-coupled network of bursting AIIs, hyperpolarizing a single cell by current injections did not have much effect on its oscillations; this finding was recapitulated by our model (Figure 2.14). In our model of a single AII cell, the bursting frequency was sensitive to a hyperpolarizing current injection, and when the cell was hyperpolarized to around -70mV by a current injection of -15pA, the AII cell became quiescent (Figure 2.14B(i)). However, when the model AII cells were coupled to each other to form a 7x7 network of AII cells and a current of -45pA was injected to the cell at (4,4), the center of the network, the cell with the current injection was hyperpolarized to $\sim$ -70 mV but still exhibited robust bursting (Figure 2.14B(ii)), consistent with experimental observations (Figure 2.14A). The bursting frequency of the hyperpolarized AII was similar to the frequency before the current injection, due to its coupling to other bursting AII cells. In this simulation, the gap junction coupling of 700pS was placed at the soma compartment of the AII model in order to capture the gap junctions localized at dendrites.

Figure 2.12 *(preceding page).* **The extracellular recordings of single RGCs show elimination of the oscillations under M-current blocker.**
A. A representative single unit. (i) Raster plots under L-AP4, LP, and wash-out conditions of a representative single unit and their (ii) interspike interval distributions with 15 ms and 30ms bin sizes for L-AP4/wash-out and LP conditions, respectively. Under LP condition, the nonzero peak of the interspike interval distribution occurs around 810 ms, which is significantly higher than under L-AP4 (180 ms) and wash out (210 ms). The raster plot under LP also shows slower rhythmic activity compared to L-AP4 and wash out conditions. **B**. Single unit bursting statistics. (i) Mean burst length for L-AP4, LP, and wash out conditions. (ii) Oscillation frequency for L-AP4, LP, and wash out conditions.

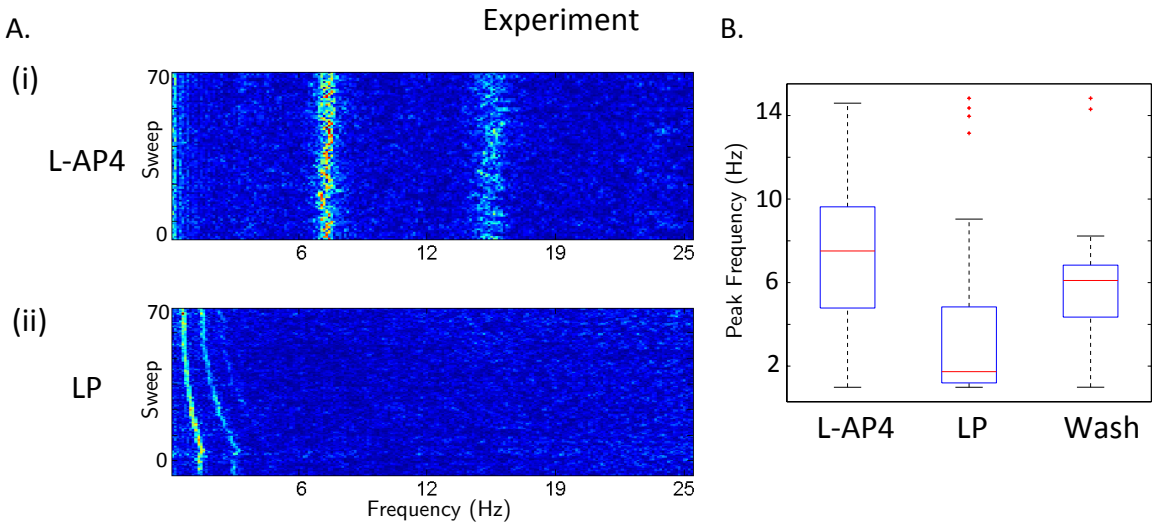

Figure 2.13. **The multi-unit activity of the extracellular recordings shows dependency of the RGC oscillations on M-current.** Multi-unit activity oscillation analysis. **A**. Example channel MUA oscillations under L-AP4 and LP conditions. The spectrograms are in 5 second-long sweeps with a 2.5 second overlap. For the MUA, 52 channels had oscillatory activity for the L-AP4 condition. 70 channels had oscillatory activity for the LP condition, and 66 channels had oscillatory activity for the wash out condition. **B**. Boxplot of MUA oscillation frequencies under L-AP4, LP, and wash-out conditions.

Also, the slow time scale of bursting allows bursting to spread efficiently across the gap-junction coupled network of AII and ONCB cells. It has been found that the local field potentials (LFPs) propagate across the retina [**47**]. As the LFPs are believed to arise from the rhythmic inputs to the RGCs from the presynaptic cells [**47**], the gap junction coupling among the AII amacrine cells may be responsible for the propagation of the LFPs. In order to see whether such propagation of rhythmic activities can be observed in the coupled network of AII cells, a 10×10 lattice of electrically coupled AII cells was simulated. In the network, slight heterogeneities were introduced in the

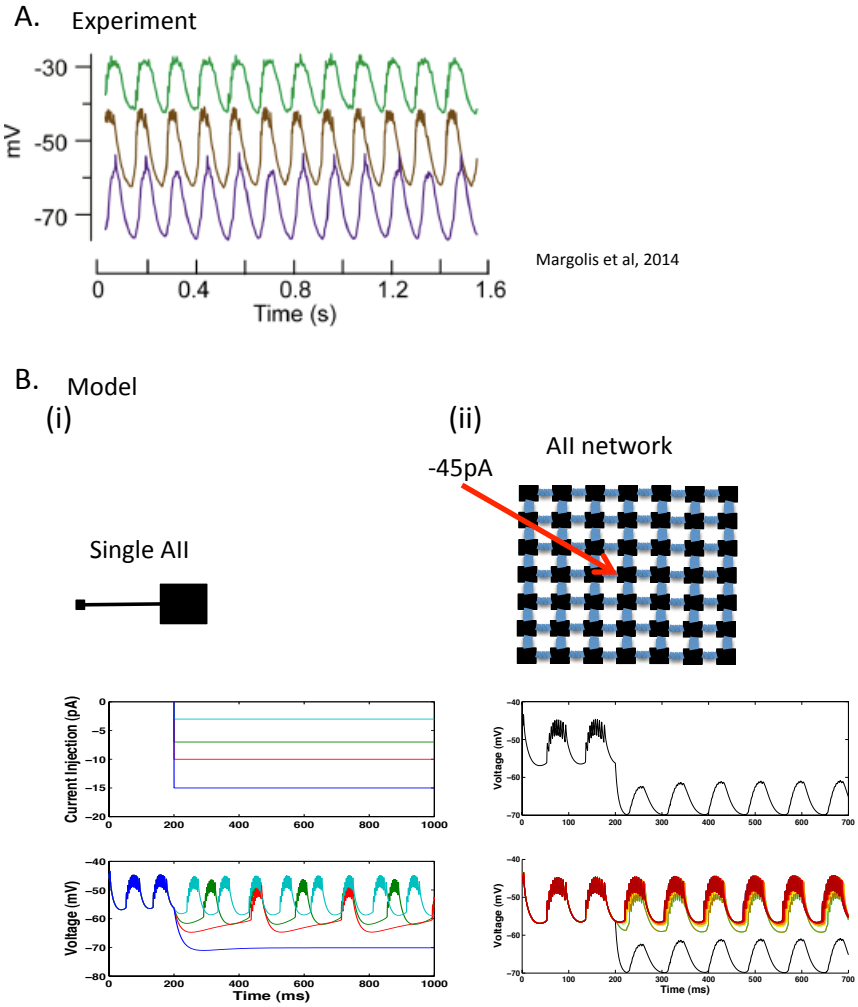

Figure 2.14. **Gap junction coupled network of AIIs shows robust rd1 oscillations**
A.Experiments show that the rd oscillations recorded from an AII cell are largely invariant under hyperpolarizing current injections. The figure is from Margolis et al, 2014 [**45**]. **B**.Simulations of hyperpolarizing current injections to a single AII cell (i) and the cell at the center of a 7x7 network of electrically coupled AII cells (ii). The current injections occur at $t = 200$ms.

maximal active conductances (within 10%) and in the parameters for the Na- and K-current kinetics (within 5%). Specifically, the values of $\bar{g}_{IS,Na}$, $\bar{g}_{IS,M}$, $\bar{g}_{IS,A}$ and $\bar{g}_{soma,A}$, were randomly chosen from a uniform distribution within $\pm 10\%$ of the original values introduced in Chapter 2.2.1.1. The values of $V_{1/2,h_{Na}}$, $V_{1/2,m_{Na}}$, $k_{h_{Na}}$, $k_{m_{Na}}$, $\tau_{h_{Na}}$, $\tau_{m_{Na}}$, $V_{1/2,m_M}$, k_{m_M}, τ_{m_M}, $V_{1/2,m_A}$, $V_{1/2,h_A}$, k_{h_A}, k_{m_A}, and τ_{m_A} were randomly chosen from a uniform distribution within $\pm 5\%$ of the original values. The AII cells were coupled to neighboring AIIs on a 10×10 square lattice with a coupling strength of 700pS.

The propagation of the LFPs may involve mechanisms other than the electrical coupling between AIIs, as the LFPs do not directly reflect the rhythmic activity in the AIIs. For example, the signal propagation from the AIIs to the ganglion cells are not counted in our simulations. Therefore, our simulation of the network of coupled AIIs is not enough to provide refined predictions on the propagation of the LFPs observed in [**47**]. However, the simulation captured qualitative aspects of the experimentally observed LFP propagation; similar to the LFP propagation observed from rd1 retinas (Figure 2.15A), synchronized rhythmic activity propagated across the AII network model (Figure 2.15B(i)). Therefore, the electrical coupling between AIIs may be responsible for the propagation of LFPs in the rd1 retina.

Furthermore, in a one-dimensional ring of 20 electrically coupled model AII cells, synchronized oscillations between the neighboring cells were observed (Figure 2.15B(ii)). In this simulation, the AIIs were mildly heterogeneous as in the previous simulation of the lattice of AIIs, and the coupling strength was 800 pS. These simulations suggest that the electrical coupling among AII cells may contribute to synchronization and propagation of the rd1 oscillations.

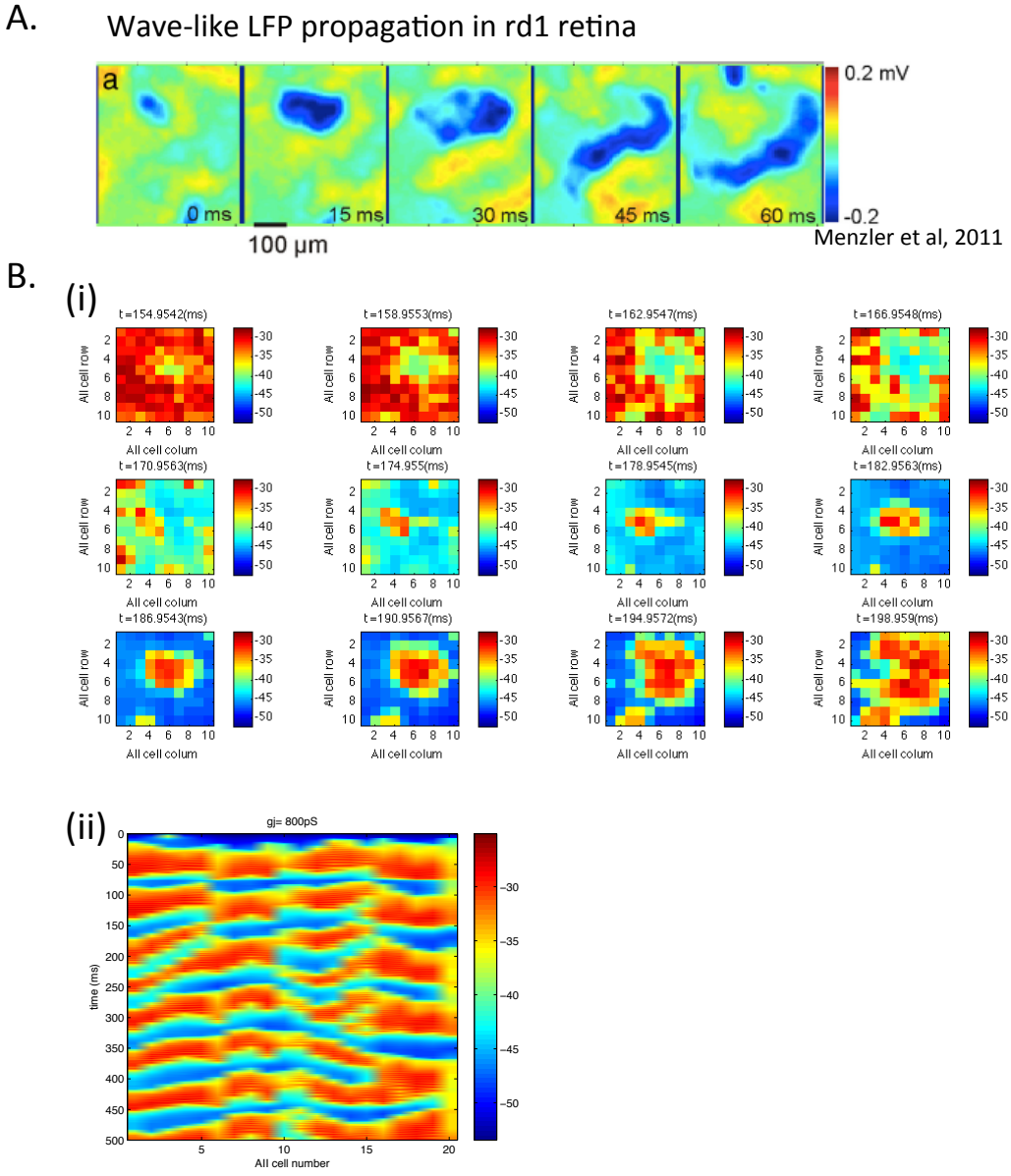

Figure 2.15. **Gap junction coupled network of AIIs contributes to propagation and synchronization of the rd oscillations.**
A. Propagation of LFPs in the rd1 retina. From Menzler et al, 2011.[**47**]
B. Simulations (i) A 10x10 network of coupled AII cells with the electrical coupling strength 700pS. (ii) 20 AII cells coupled to form a ring with the coupling strength 800pS.

2.4.3. Bursts in wt retina

We have found that the rd1 oscillations arise from bursting AIIs that merely are more hyperpolarized than those in wt retina. This raises the question whether the AIIs in the wt retina might signal by bursting as well as by spiking tonically. In particular, bursts in wt AIIs could be useful in transmitting signals across gap junctions. Since the gap junctions represent low-pass filters [**71**] bursts are more efficiently communicated through gap junctions than individual spikes. Therefore, a transition from tonic spiking to bursting may function as a switch that triggers propagation of Na-mediated activity across gap junctions.

CHAPTER 3

Bifurcation analysis of bursting in a model of AII amacrine cells

Bifurcation theory has served as a powerful tool for understanding various nonlinear dynamical systems. Models of neurons are one set of examples, and bifurcation analysis has helped unravel various neuronal activities. Diverse patterns of activity observed in neurons, such as tonic spiking and bursting, have been associated with different functions in signal processing, and transitions from one state to another may have significant functional implications in the nervous system. In our work from the previous chapter, the three-compartment model of single AII amacrine cell was successful in capturing both tonic spiking and bursting observed experimentally in the rd1 and wildtype retina. Here we apply bifurcation theory to analyze the dynamics of the AII amacrine cell. We first apply the method of fast-slow analysis to elucidate the bursting mechanism, and extend the analysis to probe the transition between the tonic spiking and bursting modes in the AII amacrine cell. We show that the burster is a fold/fold type in the fast subsystem, and the transition from tonic spiking to bursting involves a torus bifurcation. An averaging technique was implemented to explain the emergence of tonic spiking and bursting. Furthermore, the system demonstrates coexistence of tonic spiking and bursting.

3.1. Introduction

Neurons, as nonlinear dynamical systems, can exhibit various patterns of activity such as tonic spiking and bursting. The various patterns of neural activity play important

functional roles, including coding of sensory information, memory formation, attention, information processing and motor control. By studying a mathematical model of a single neuron, we can gain insights into the generation of these dynamical patterns as well as the transitions among them.

Bursting in a neuronal model has been classified by the methods of slow-fast analysis [**33, 34**]. In order for a neuronal model to exhibit bursting behavior, the model needs at least one fast variable and one slow variable, and can be described by

$$\dot{x} = F(x, z), \tag{3.1}$$

$$\dot{z} = \epsilon G(x, z) \tag{3.2}$$

where $\epsilon \ll 1$. $x \in \mathbb{R}^m$ describes relatively fast processes that generate action potentials, and $z \in \mathbb{R}^k$ describes relatively slow processes associated with modulation. By setting $\epsilon = 0$, the fast subsystem x can be decoupled from the slow subsystem z. Once decoupled, the slow variable becomes a parameter in the fast subsystem. The decoupled fast subsystem, where $\epsilon = 0$, provides insights into the behavior of the whole system where $0 < \epsilon \ll 1$ as well. A trajectory of the whole system where $0 < \epsilon \ll 1$ converges exponentially fast to the chosen attracting branch composed of either fixed points or limit cycles, so that its slow-coordinate remains close to the starting point. Once nearby, the trajectory moves along the branch with the rate of change in the direction of the slow variable of order ϵ [**21**].

In the fast subsystem, bursting can be viewed as alternation between a tonic spiking regime and a quiescent regime. Neuronal bursters have been classified by how the fixed points (quiescent regime) and the limit cycles (tonic spiking regime) lose stability in the

decoupled fast subsystem in [**33, 34**]. For example, "Fold/Hopf" burster refers to the fast-slow bursting in which the rest state disappears via a fold bifurcation and the repetitive spiking disappears via a supercritical Hopf bifurcation in the fast subsystem.

Decoupling the fast and slow subsystems provides simple and straightforward analysis of neuronal dynamics. However, more complicated and interesting phenomena can be explained by studying the full system where $\epsilon \neq 0$. A good example that requires consideration of the full system is the transition between the tonic spiking regime and the bursting regime.

In this chapter, we explore the bursting mechanism using the method of fast-slow analysis as well as the transition between the tonic spiking mode and the bursting mode in the three-compartment model of AII amacrine cell. In the previous chapter, we have shown that the characteristic oscillations that arise under the pathological condition of retinal degeneration originate from bursting in individual AII amacrine cells. Moreover, the wildtype AII amacrine cell, which normally spikes tonically, undergoes a transition to spontaneous bursting when hyperpolarized, suggesting that the AIIs in the wildtype retina might signal by utilizing both modes. Therefore, understanding the transition from tonic spiking to bursting should expand our knowledge on the signal processing in the AII amacrine cell. Throughout this chapter, the continuation of fixed points and periodic orbits of the model is carried out by the software packages XPPAUT and MATCONT.

3.2. Fast-slow analysis of the AII bursting

The three-compartment model of AII amacrine cell from Chapter 2 replicates tonic spiking and bursting observed experimentally. In particular, we have previously shown

that cable-filtered bursting generated in the electrotonically distal initiation site compartment underlies the rd1 oscillations. The bursting mechanism in the AII model was further investigated using the method of fast-slow analysis. Our model, described in detail in Section 2.2.1.1, has two relatively slow variables, namely, the M-type K current activation variable m_M and the A-type K current inactivation variables $h_A^{(1,2)}$. We have confirmed that freezing the A-type inactivation has negligible effects on the bursting dynamics of the AII cell model, and fixed the A-type inactivation at $h_{\infty,A}$. Then the model of AII cell is now reduced to a system of differential equations:

$$C_j \frac{dV_j}{dt} = -i_{m,j} + i_{section,j},\ (j = 1, 2, 3) \tag{3.3}$$

$$\tau_{m_{Na}} \frac{dm_{Na,j}}{dt} = m_{\infty,Na}(V_j) - m_{Na,j},\ (j = 3) \tag{3.4}$$

$$\tau_{h_{Na}} \frac{dh_{Na,j}}{dt} = h_{\infty,Na}(V_j) - h_{Na,j},\ (j = 3) \tag{3.5}$$

$$\tau_{m_M} \frac{dm_{M,j}}{dt} = m_{\infty,M}(V_j) - m_{M,j},\ (j = 3) \tag{3.6}$$

$$\tau_{m_A} \frac{dm_{A,j}}{dt} = m_{\infty,A}(V_j) - m_{A,j},\ (j = 1, 3). \tag{3.7}$$

where

$$i_{m,j} = i_{leak,j} + i_{Na,j} + i_{m,j} + i_{A,j} \tag{3.8}$$

$$i_{section,j} = \bar{g}_{j,j+1}\left(V_{j+1} - V_j\right) + \bar{g}_{j,j-1}\left(V_{j-1} - V_j\right), \tag{3.9}$$

$\bar{g}_{j,j+1} = 0$ for $j = 3$ and $\bar{g}_{j,j-1} = 0$ for $j = 1$. Otherwise, the conductance between two neighboring compartments is given by Eq.(2.2) with Eq.(2.1). The index $j = 1, 2, 3$ refers

to the soma, the cable, and the initiation site compartment of the AII model, respectively. Details on the ionic currents and the parameters can be found in Section 2.2.1.1. In order to apply the method of fast-slow analysis, we need to identify the slow variables and the fast variables, as in Equations (3.1) and (3.2). In this model, m_M in the initiation site, with $\tau_{m_M} = 50$ ms, is the only slow variable. Therefore, with a time constant $\tau \ll \tau_{m_M}$ where τ corresponds to a fast time scale (comparable to $\tau_{m_{Na}}$, $\tau_{h_{Na}}$, and τ_{m_A}), m_M, τ/τ_{m_M}, and $m_{\infty,M}(V) - m_M$ correspond to z, ϵ, and $G(x, z)$ in Equation (3.2), respectively. The rest of the variables belong to the fast process. Thus, decoupling the fast subsystem from the slow subsystem involves fixing m_M and treating it as the bifurcation parameter.

The continuation with m_M as the bifurcation parameter in the fast subsystem was carried out to yield the bifurcation diagrams in Figure 3.1A. The stable fixed points lose stability at a fold bifurcation (also called saddle-node or limit point) around $m_M = 0.13$ and via a supercritical Hopf bifurcation around $m_M = 0.086$. The stable limit cycles emerge from the Hopf bifurcation, lose stability via a fold bifurcation, then regain stability via another fold bifurcation at $m_M = -0.036$. Although in reality m_M is confined between 0 and 1 and cannot be negative, extending the parameter range allows us to see the full bifurcation structure. The stable limit cycles correspond to the spiking phase in the AII burster. During the spiking phase, the M-current gets activated and the trajectory moves in the direction of increasing m_M. When the limit cycle is annihilated by the unstable limit cycle at the fold bifurcation again at $m_M = 0.19$, the trajectory falls down to the branch of stable fixed points, which correspond to the quiescent phase of bursting. The quiescence then deactivates the M-current, thus the solution evolves along the fixed-point branch, and when the fold of the fixed point branch is reached at $m_M = 0.13$, the system

is attracted to the stable limit cycle branch reinitiating the spiking phase. This bursting mechanism explained by the bifurcation diagram in the fast subsystem closely matches in terms of ranges of variables with the dynamics of the variables V_{soma}, V_{IS}, and m_M in the full system of a bursting AII cell (Figure 3.1B).

3.3. Transition between tonic spiking and bursting

Next, we investigated a transition between tonic spiking and bursting using the full system where $\epsilon \neq 0$. Here, m_M was no longer fixed; it was described by the differential equation 3.6. Instead of m_M, now the maximal M-type K conductance $\bar{g}_M$ was chosen as the bifurcation parameter. At low $\bar{g}_M$, the AII model exhibits tonic spiking. As $\bar{g}_M$ increases, the slow modulation gets stronger, and the model undergoes a transition to bursting. These two modes of firing are manifested in Figure 3.2A(i),B(i); at $\bar{g}_M = 0.02(S/cm^2)$, the full system exhibits tonic spiking, while at $\bar{g}_M = 0.04(S/cm^2)$ it shows bursting.

In order to elucidate how different values of $\bar{g}_M$ change the attracting mode between tonic spiking and bursting for the full system, the averaging method was employed [**55**]. In our model of the AII amacrine cell, the slow variable m_M is described by

$$\frac{dm_M}{dt} = \frac{1}{\tau_{m_M}}(m_{\infty,M}(V) - m_M) \tag{3.10}$$

Defining $G(V, m_M) = m_{\infty,M}(V) - m_M$, the averaged slow system is $\langle m'_M \rangle = \langle G(V, m_M) \rangle$ at order of $\frac{1}{\tau_{m_M}}$. On the fixed points, $\langle G \rangle$ is simply $m_{\infty,M}(V) - m_M$. On the limit cycle branch, it has to be averaged over the period of the corresponding limit cycle, and is

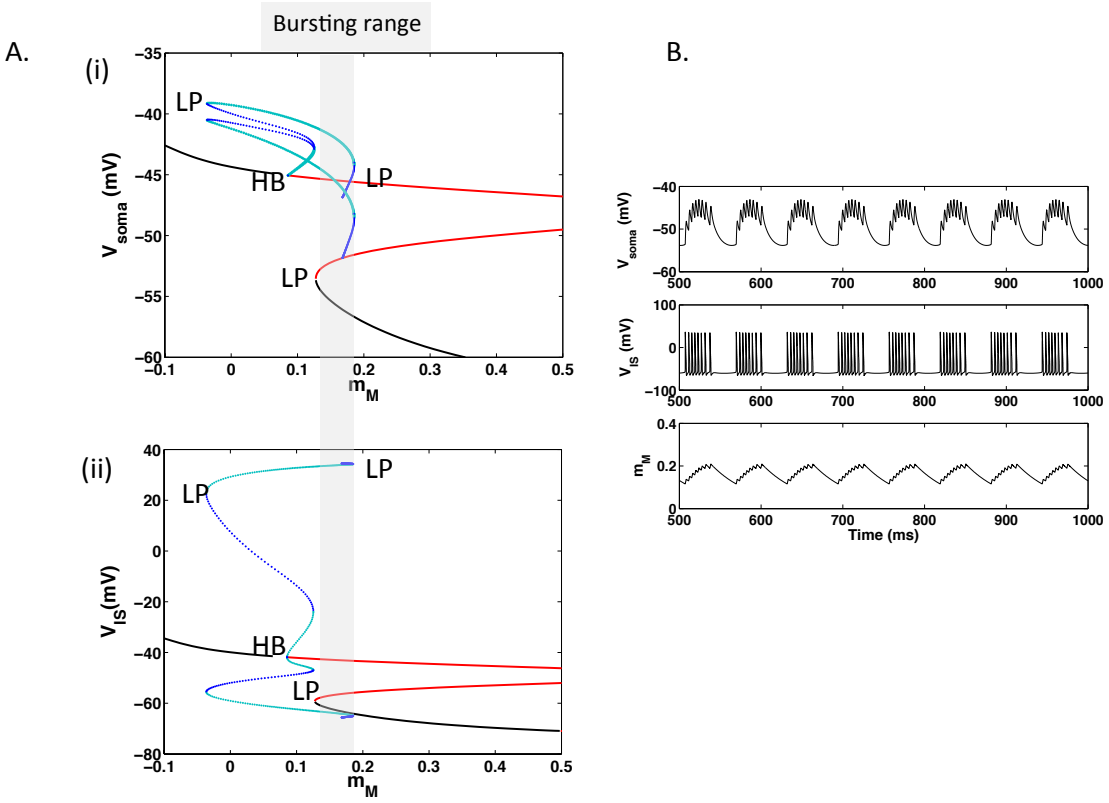

Figure 3.1. **Fast-slow analysis of bursting in the AII model**
A. Bifurcation diagram of the decoupled fast subsystem, with the M-type current activation variable m_M as the bifurcation parameter. Both the fixed points and the limit cycles lose stability via a fold bifurcation. The color representations are: black- stable fixed points, red- unstable fixed points, cyan- stable limit cycles, blue- unstable limit cycles. The limit cycle branch was followed starting from the Hopf bifurcation until the unstable limit cycle that arises at $m_M = 0.19$ via a fold bifurcation exhibited a rapid increase in period to significantly larger values and XPPAUT failed to continue along the branch. For the limit cycles, both the maxima and the minima are plotted. HB refers to Hopf bifurcation, LP refers to limit point (fold, saddle-node). The bifurcation diagram is shown as both V_{soma}-m_M plot (i) and V_{IS}-m_M plot (ii). Shaded region, where both the stable limit cycles and the stable fixed points coexist, is the bursting range. **B**. Dynamical variables in the bursting AII model. Top panel shows the voltage in the soma, middle panel shows the voltage in the initiation site, and the bottom panel shows the M-type current activation variable m_M.

defined as

$$\langle G\rangle = \frac{1}{T(m_M)}\int_0^{T(m_M)} G(v_{lc}(\tau; m_M), m_M)d\tau \tag{3.11}$$

where $v_{lc}(\tau; m_0)$ is the voltage on a $T(m_0)$-periodic stable orbit of the fast subsystem at $m_M = m_0$ and $t = \tau$. If $\langle G(v_{lc}(\tau; m_M), m_M)\rangle > 0$ on the stable limit cycle branch over a period $T(m_M)$, then the solution follows the branch in the direction of increasing m_M. If $\langle G(v_{lc}(\tau; m_M), m_M)\rangle < 0$, then the trajectory moves in the direction of decreasing m_M. In other words, the variables evolve along the stable limit cycles in the direction of increasing or decreasing m_M, depending on whether $\langle G\rangle$ is positive or negative.

Along the stable limit cycle branch and the stable fixed points, $\langle G\rangle$ was calculated and plotted as a function of m_M for the tonic spiking case where $\bar{g}_M = 0.02(S/cm^2)$ and the bursting case where $\bar{g}_M = 0.04(S/cm^2)$ in Figure 3.2A(ii),B(ii). When $\bar{g}_M = 0.02(S/cm^2)$, $\langle G\rangle$ along the stable limit cycles changes from positive to negative before the limit cycles cease to exist. At the m_M value where $\langle G\rangle$ crosses 0, therefore, the attracting limit cycle exists. The trajectory stays on the attracting limit cycle, and therefore tonic spiking is manifested. On the other hand, when $\bar{g}_M = 0.04(S/cm^2)$, $\langle G\rangle$ is always positive on the stable limit cycle branch. Thus, there does not exist an attracting limit cycle as in the case with $\bar{g}_M = 0.02(S/cm^2)$, and the trajectory always moves rightward in the increasing m_M direction on the stable limit cycle branch until it reaches the fold and jumps down to the fixed points.

Interestingly, for a certain range of $\bar{g}_M$, tonic spiking and bursting coexist in the model of AII cell. Figure 3.3 shows that for $\bar{g}_M = 0.034(S/cm^2)$, the model can either exhibit spiking or bursting depending on the initial conditions. By increasing and decreasing

A.

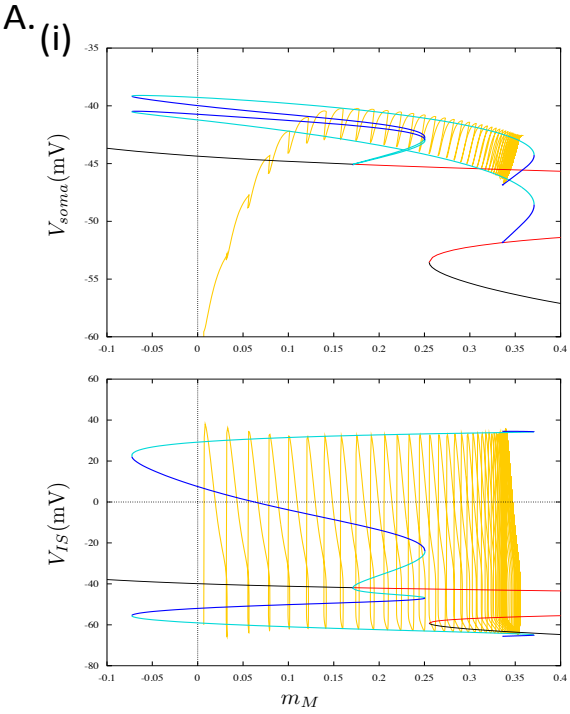
(i)
V_{soma}(mV)
V_{IS}(mV)
m_M

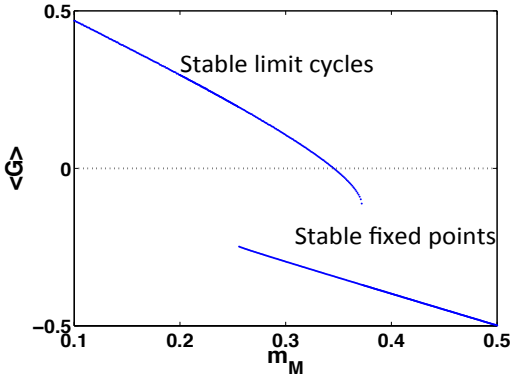
(ii)
Stable limit cycles
Stable fixed points
<G>
m_M

B.

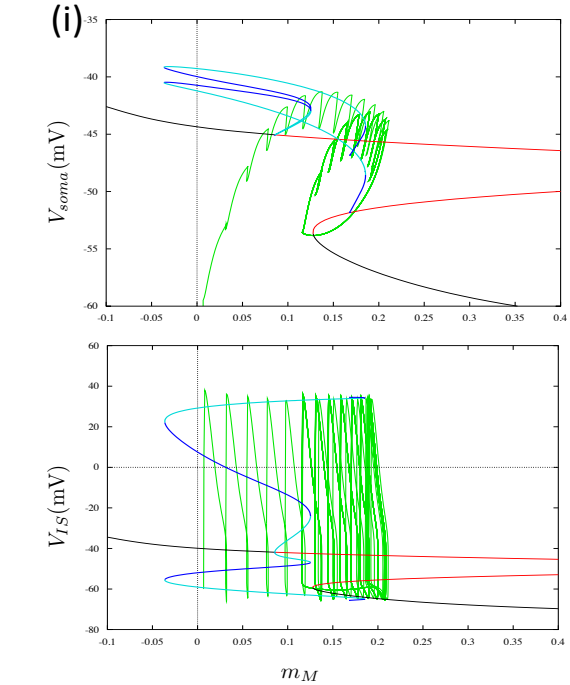
(i)
V_{soma}(mV)
V_{IS}(mV)
m_M

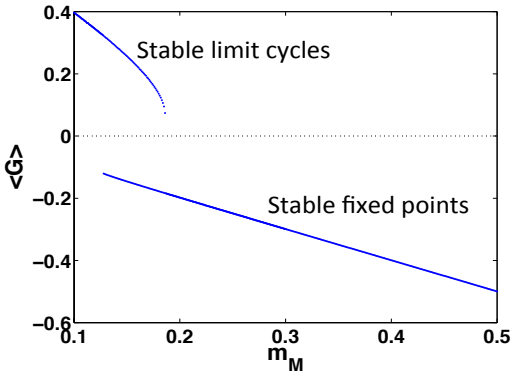
(ii)
Stable limit cycles
Stable fixed points
<G>
m_M

$\bar{g}_M$ in step increments, we sought the specific range in $\bar{g}_M$ where the bistability of tonic spiking and bursting is observed. $\bar{g}_M$ was increased and decreased within the range from $\bar{g}_M = 0.03(S/cm^2)$ to $\bar{g}_M = 0.045(S/cm^2)$ in step increments of $\Delta\bar{g}_M = 0.0001(S/cm^2)$. By plotting the maximal V_{soma} for a given value of $\bar{g}_M$ for each spike (Figure 3.4B), we can discriminate tonic spiking from bursting. As $\bar{g}_M$ decreases, the number of spikes per burst increases, and eventually the transition from bursting to tonic spiking occurs. By comparing the diagram to the case where the $\bar{g}_M$ is increased, we found that over the range from $\bar{g}_M = 0.0323$ to $\bar{g}_M = 0.0365(S/cm^2)$, tonic spiking and bursting coexist.

By continuing in the full system with $\bar{g}_M$ as the bifurcation parameter using XPPAUT, a torus bifurcation (also called secondary Hopf or Neimark-Sacker) was detected at $g_{M,IS} = 0.03647(S/cm^2)$. This closely matches with the $\bar{g}_M$ value where the tonic spiking goes through a transition to bursting in the AII model (Figure 3.5A). When $\bar{g}_M$ was increased in step increments of $\Delta\bar{g}_M = 0.0001(S/cm^2)$, the system switched from the tonic spiking mode to bursting at the step $\bar{g}_M = 0.0365(S/cm^2)$. Moreover, at this $\bar{g}_M$ step, the dynamical variables, including V_{soma} (Figure 3.5B), showed modulated tonic

---

Figure 3.2 *(preceding page)*. **Averaged slow equation explains the transition between tonic spiking and bursting.**
A. At $\bar{g}_M = 0.02(S/cm^2)$, the AII model exhibits tonic spiking. (i) The phase diagram of the full system (yellow) with random initial conditions plotted over the bifurcation diagrams in the fast subsystem (top: V_{soma}-m_M, bottom: V_{IS}-m_M). The full system asymptotes to a single limit cycle that corresponds to tonic spiking. (ii) The averaged slow equation $\langle G \rangle$ as a function of m_M. $\langle G \rangle$ represents the averaged rate of change in m_M along the stable branchs. $\langle G \rangle$ along the stable limit cycles crosses 0 before the limit cycles lose stability. **B**. At $\bar{g}_M = 0.04(S/cm^2)$, the AII model exhibits bursting. (i) The phase diagram of the full system (green) with random initial conditions plotted over the bifurcation diagrams in the fast subsystem (top: V_{soma}-m_M, bottom: V_{IS}-m_M). (ii) $\langle G \rangle$ along the stable limit cycles stays positive and does not cross 0 before the limit cycles lose stability.

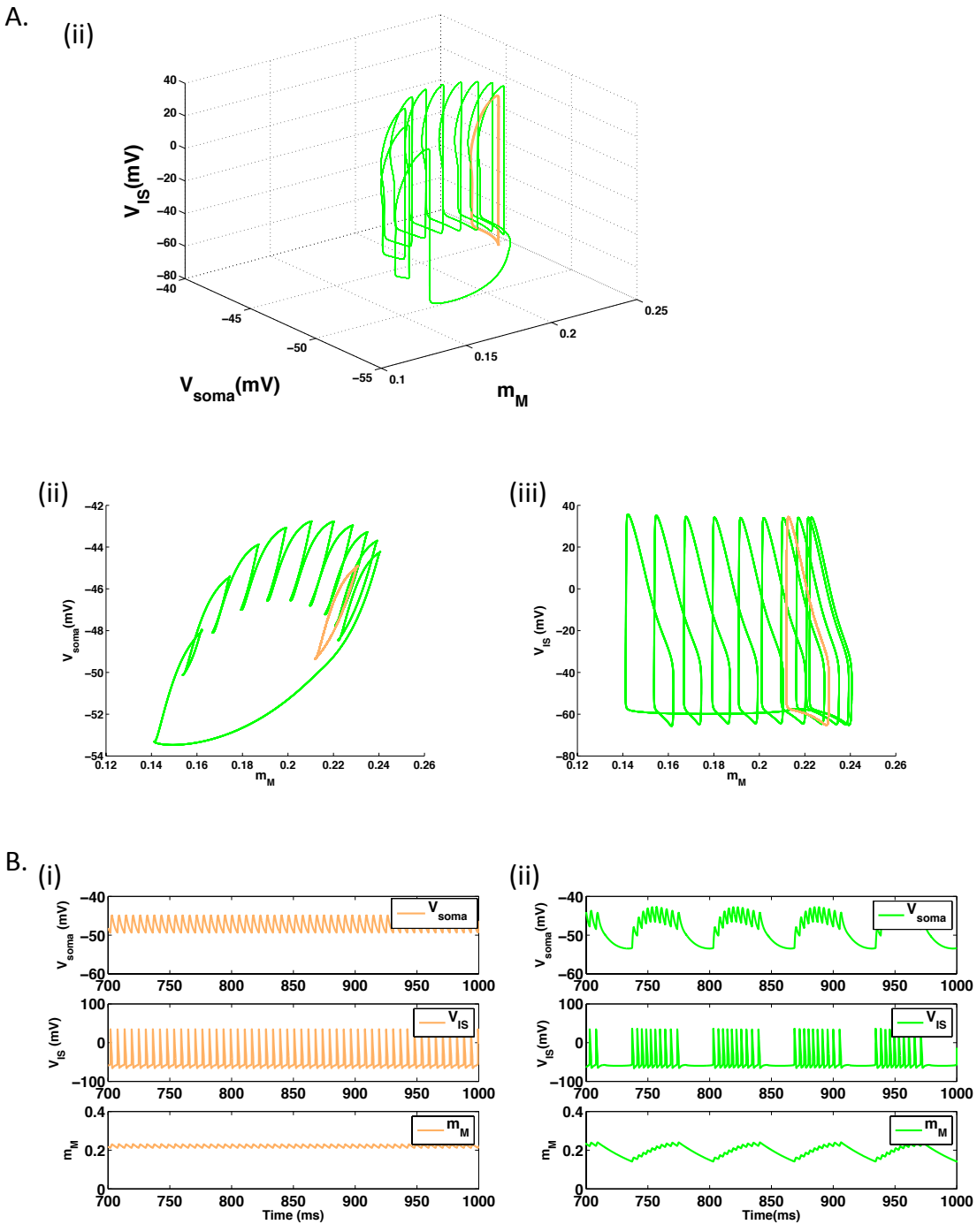
A.
(ii)
V_IS(mV)
V_soma(mV)
m_M
(ii)
(iii)
V_soma (mV)
V_IS (mV)
m_M
B.
(i)
(ii)
V_soma
V_IS
m_M
Time (ms)
Time(ms)

spikes that grow faster than exponentially in amplitude, and eventually made a rapid transition to bursting. Along with the existence of hysteresis between tonic spiking and bursting, this is consistent with the torus bifurcation between tonic spiking and bursting being subcritical.

In order to test whether the averaged slow system can explain the bistability as in the leech heart neuron model from [**56**], we calculated $\langle G \rangle$ and plotted it as a function of the M-current activation m_M at $\bar{g}_M = 0.034(S/cm^2)$, where our simulations show coexistence of bursting and tonic spiking (Figure 3.6B). However, $\langle G \rangle$ along the limit cycle branch does not cross 0 twice to divide the region into the bursting regime and the tonic spiking regime as in [**56**], and the method of averaging thus does not explain the bistability.

Moreover, the bistability does not arise from the A-type K activation variable in the soma, $m_{A,soma}$, as the range of $\bar{g}_M$ where tonic spiking and bursting coexist is shifted but continues to exist when the A-type K activation variable $m_{A,soma}$ does not vary in

---

Figure 3.3 *(preceding page).* **Coexistence of tonic spiking and bursting in the AII model**
For the same maximal M-type K conductance $\bar{g}_M = 0.034(S/cm^2)$, the model AII cell exhibits either tonic spiking (yellow) or bursting (green) depending on the initial conditions. **A**. (i) Coexistence of bursting and tonic spiking in the (m_M, V_{soma}, V_{IS})-space. In the (m_M, V) projection for the voltage in the soma (ii) and the voltage in the IS (iii), the small periodic orbit corresponds to the tonic-spikes and the large complex cycle corresponds to the bursting shown in **B**.(i),(ii), respectively. In **B**., the top panel shows the voltage in the soma, the middle corresponds to the voltage in the IS, and the bottom figure shows m_M. The initial condition that corresponds to the tonic spiking is ($m_{A,soma}$,V_{soma}, V_{cable}, m_{Na}, h_{Na}, $m_{A,IS}$, V_{IS})=(0.0058,-46.0509, -54.8832, 0.0413, 0.7975, 0.1459, 0.2279, -63.6892), and the initial condition that leads to the bursting is ($m_{A,soma}$,V_{soma}, V_{cable}, m_{Na}, h_{Na}, $m_{A,IS}$, V_{IS})=(0.0024, -52.3297, -56.0457, 0.0856, 0.9942, 0.0008, 0.1861, -59.8424).

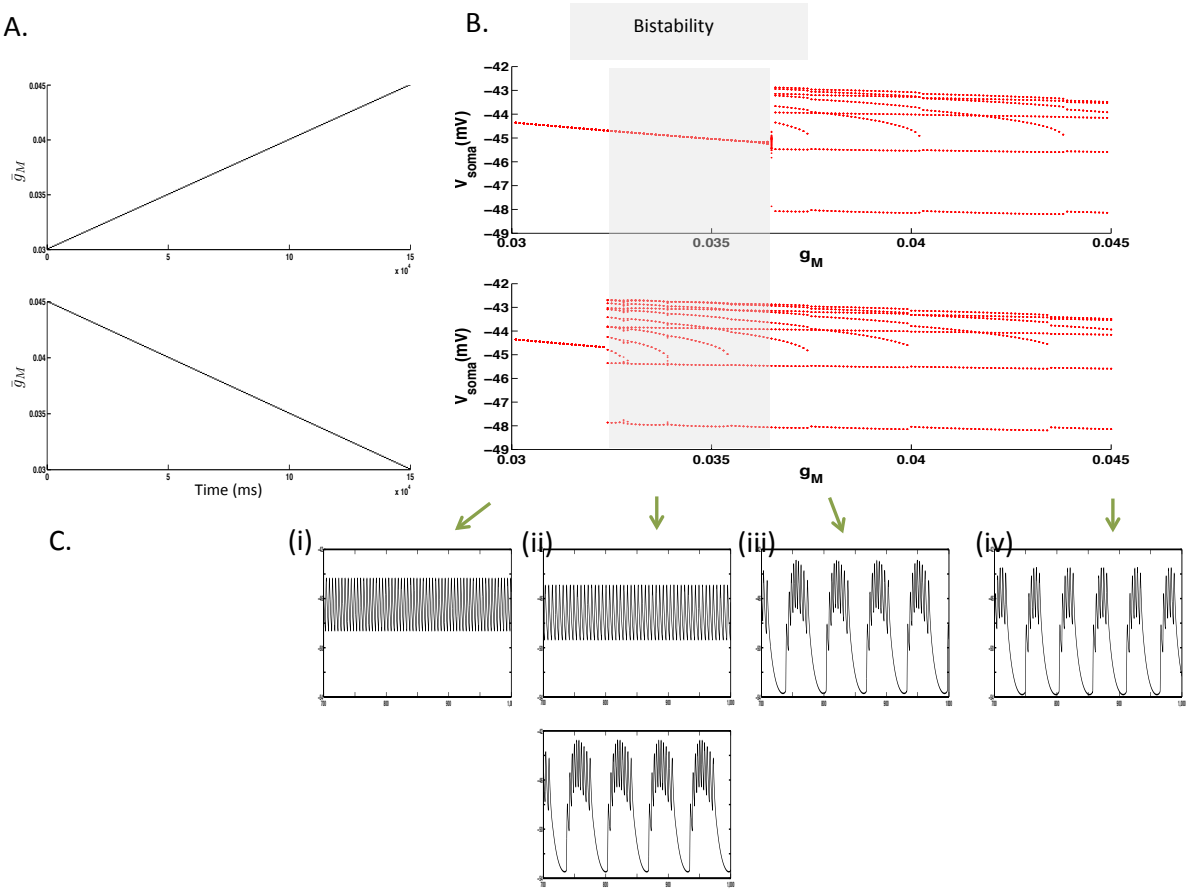

Figure 3.4. **Bistability of tonic spiking and bursting was observed over a small range of $\bar{g}_M$.**
A. The maximal M-type K conductance $\bar{g}_M$ was increased (top) and decreased (bottom) in step increments of $\Delta\bar{g}_M = 0.0001(S/cm^2)$, with $\bar{g}_M$ ranging from 0.03 to $0.045(S/cm^2)$. Each step is 1s-long. **B**. Local maxima from each spike in burst, measured in somatic voltage, are plotted as $\bar{g}_M$ is increased (top) and decreased (bottom). As each dot corresponds to a spike in the IS, tonic spiking corresponds to a single point and bursting to a series of points. As $\bar{g}_M$ decreases, the number of spikes per burst increases, and at a certain $\bar{g}_M$, tonic spiking emerges. As $\bar{g}_M$ increases, tonic firing undergoes a transition to bursting, but there exists a range of $\bar{g}_M$ where both modes of firing coexist (gray shade). **C**. Traces of V_{soma} at various $\bar{g}_M$ that correspond to the points in B. (i) At $\bar{g}_M = 0.03(S/cm^2)$, only tonic spiking exists. (ii) At $\bar{g}_M = 0.034(S/cm^2)$, tonic spiking and bursting modes are bistable. (iii) At $\bar{g}_M = 0.037(S/cm^2)$, only bursting can be observed. (iv) As $\bar{g}_M$ increases further, at $\bar{g}_M = 0.045(S/cm^2)$, fewer number of spikes occur per burst.

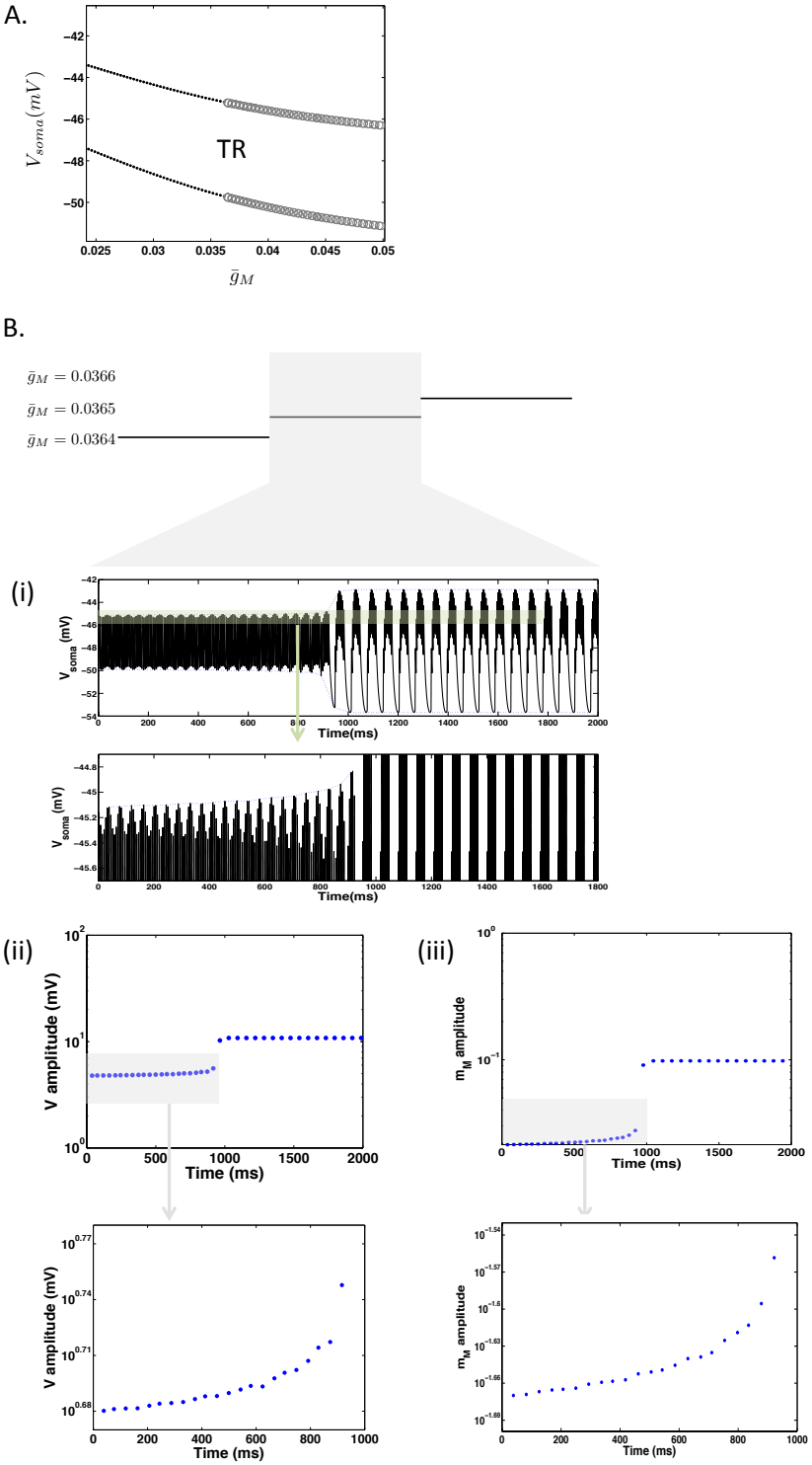
A.
TR
$V_{soma}(mV)$
$\bar{g}_M$
B.
$\bar{g}_M = 0.0366$
$\bar{g}_M = 0.0365$
$\bar{g}_M = 0.0364$
(i)
V_{soma} (mV)
Time(ms)
(ii)
V amplitude (mV)
Time (ms)
(iii)
m_M amplitude
Time (ms)

time in the soma (Figure 3.7). In this simulation, $m_{A,soma}$ was fixed at $m_{\infty,A}$ as given by Eq.(2.17) with $V = -57$ (mV).

The range of $\bar{g}_M$ where the coexistence of tonic spiking and bursting occurs decreases as the M-current activation time constant τ_{m_M} increases (Figure 3.8). The bistability may disappear, therefore, in the limit $\tau_{m_M} \to \infty$, namely, in the fast-slow limit $\epsilon \to 0$. Thus, the decoupled fast subsystem where $\epsilon = 0$ may not provide a sufficient basis to explain the bistability of tonic spiking and bursting.

3.4. Discussion

In this chapter, we studied two representative dynamics – tonic spiking and bursting — that arise in a compartmental model of the AII, using bifurcation theory. The method of fast-slow analysis revealed the bursting mechanism in the decoupled fast subsystem. In the fast subsystem, there is a hysteresis between the stable limit cycles and the stable fixed points, where both the limit cycles and the fixed points cease to exist at saddle-node bifurcations. Moreover, continuation in the maximal M-type K conductance $\bar{g}_M$ in the

---

Figure 3.5 *(preceding page).* **Tonic spiking mode makes a transition to bursting via a torus bifurcation.**
A. XPPAUT detects a torus bifurcation at $\bar{g}_M = 0.03647(S/cm^2)$. TR denotes torus bifurcation, black solid circles represent stable limit cycles, and gray open circles represent unstable limit cycles. Both maxima and minima of the limit cycles are plotted. **B**. As $\bar{g}_M$ increases in step increments, the AII model switches from tonic spiking mode to bursting mode at $\bar{g}_M = 0.0365(S/cm^2)$ (i). At this $\bar{g}_M$ step, the traces of V_{soma} was plotted. The modulated tonic spikes increase in amplitude before making a transition to bursting (i). The enveloped modulation amplitude of both V_{soma} (ii) and m_M (iii) grows exponentially in the beginning, the growth gets faster, and the AII switches to bursting.

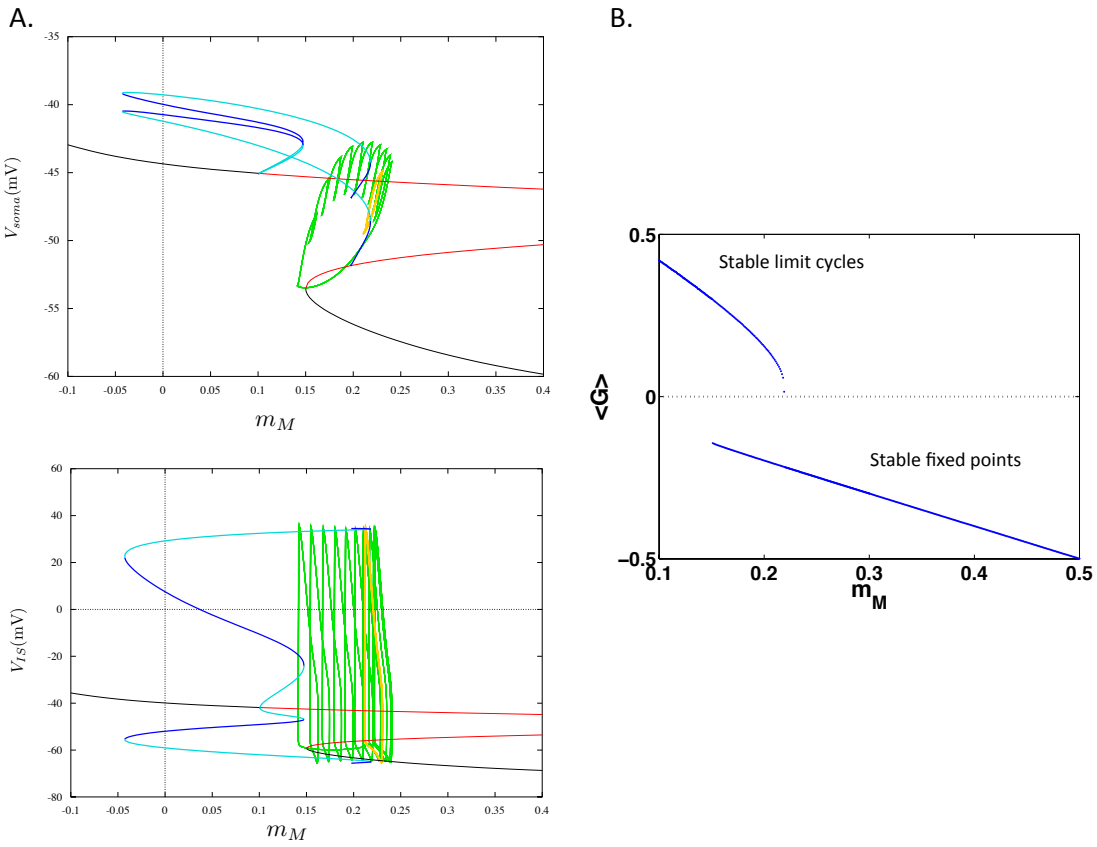

Figure 3.6. **Fast subsystem and averaged slow equation at the bistable regime where tonic spiking and bursting coexist**
At $\bar{g}_M = 0.034(S/cm^2)$.**A**. The phase digram of the full system plotted over the bifurcation diagrams in the fast subsystem (top: V_{soma}-m_M, bottom: V_{IS}-m_M). Depending on the initial conditions, the model either exhibits tonic spiking (yellow) or bursting (green). **B**. $\langle G \rangle$ as a function of m_M along the stable limit cycles and the stable fixed points.

full system demonstrated that the transition between tonic spiking and bursting occurs via a torus bifurcation.

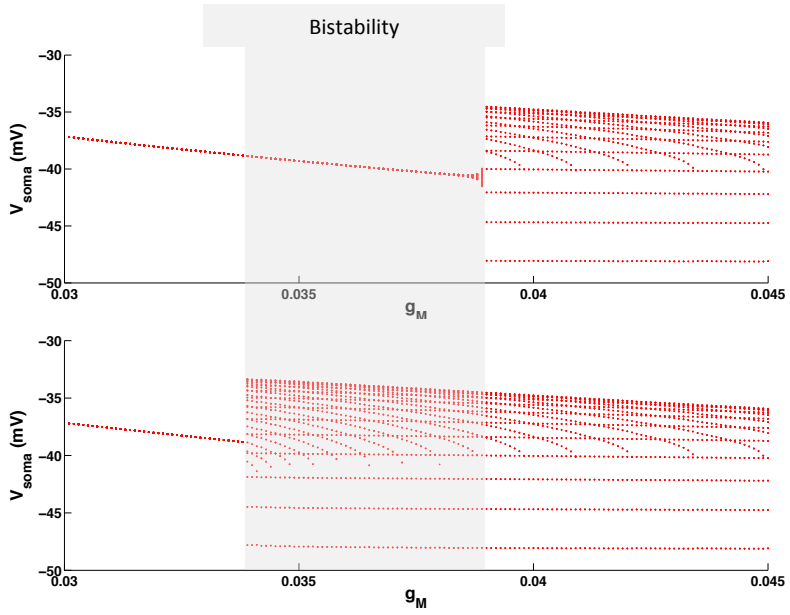

Figure 3.7. **Bistability of tonic spiking and bursting remains existing with the A-type K activation variable fixed in the soma.** $\bar{g}_M$ was increased (top) and decreased (bottom) as in Figure 3.5 . The bistability range is shifted to $\bar{g}_M = 0.0339 - 0.039(S/cm^2)$.

Our model predicts the existence of a bistable regime for a small range of the slow M-type K conductance $\bar{g}_M$ where tonic spiking and bursting coexist. Whether such bistability exists in real AII cells is not known, and experimental verification would require tight control on the M-type K conductance mediated pharmacologically, for example, by involving M-type K blockers. Whether the bistability exists in vivo or not would be an interesting question, as tonic spiking and bursting are likely play different functional roles in the signal processing in AIIs.

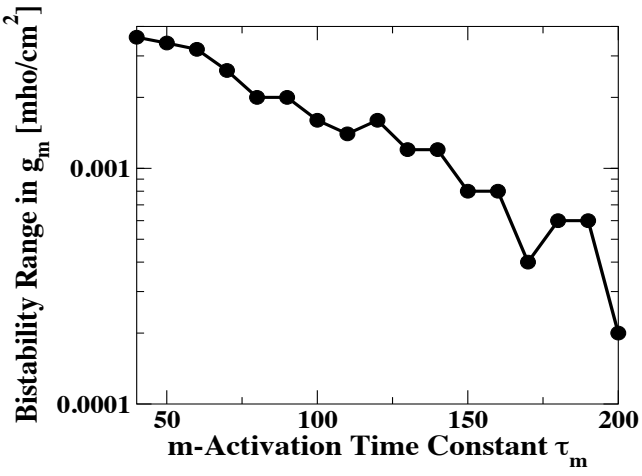

Figure 3.8. **Bistability range depends on τ_{m_M}**
The range of $\bar{g}_M$ where tonic spiking and bursting coexist decreases as $\tau_{m_M} \to 0$, possibly exponentially.

CHAPTER 4

Conclusion

In this thesis, various dynamics displayed by the AII amacrine cell, a class of retinal interneurons, have been studied. First, the mechanisms underlying the characteristic oscillations that arise in the degenerated rd1 retina were investigated based on both experimental and computational approaches. Prior to this work, it has been suggested that the characteristic oscillations arise as an emergent property of an electrically coupled network of heterogenous AIIs. Through collaboration with the Singer lab, we have found that the oscillations are generated by the intrinsic mechanisms of individual AIIs rather than by a network effect. Based on the compartmental model of AII, we predicted the role of M-type K current in the characteristic rd1 oscillations, which was confirmed by experiments. The changes in the oscillation frequency and the burst duration under M-current blockers and activators were correctly predicted by the model. In the experiments, the M-current blocker induced qualitatively different, slow Ca-dependent oscillations in the ONCBs. We have explained the mechanism of these Ca-dependent oscillations by extending our passive ONCB model to include a simple model of FitzHugh-Nagumo type. The experiments further confirmed that the rhythmic activity in the ganglion cells originates from the presynaptic AIIs, as the AII activity under the M-current blockers and activators was propagated unchanged to the ganglion cells. Thus, the rd1 oscillations observed in the inner retina are generated by the interplay between a fast, spike inducing Na current and a slow M-type K current in AII cells, as in the bursting of hyperpolarized wildtype

AIIs. Combined with the experimental recordings of the resting membrane potentials of rd1 and wildtype AIIs, we conclude that the rd1 oscillations are generated by individual AII cells that are more hyperpolarized in the rd1 retina compared to the wildtype retina. Therefore, the membrane potential of the AIIs may be a suitable pharmacological target for abolishing the oscillations observed in retinal degeneration.

Secondly, we employed bifurcation theory to explain bursting and tonic spiking in the compartmental AII model. As the AII exhibits spontaneous bursting in the degenerated retina and tonic spiking in the wildtype retina, understanding the mechanism of bursting as well as the transition between tonic spiking and bursting is not only mathematically interesting but also biologically relevant. With the M-current activation variable as the slow parameter, the fast-slow analysis has revealed that bursting in the AII model arises from the hysteresis between limit cycles and fixed points, which lose stability via saddle-node bifurcations. Moreover, our bifurcation study of the full system with the maximal M-conductance as the bifurcation parameter has shown that the transition between tonic spiking and bursting involves a torus bifurcation, and there exists a range of the maximal M-conductance where tonic spiking and bursting coexist.

As the AII amacrine cell plays a central role in the rod bipolar pathway, understanding dynamics displayed by the AII is crucial to understand signal processing in scotopic vision. Some of the open questions discussed earlier in this thesis, such as the role of the gap junction coupling among the AIIs and the mechanism underlying the bistability of tonic spiking and bursting, therefore, would be interesting subjects for future work.

References

[1] Acland, G. M., Aguirre, G. D., Ray, J., Zhang, Q., Aleman, T. S., Cideciyan, A. V., Pearce-Kelling, S. E., Anand, V., Zeng, Y., Maguire, A. M., Jacobson, S. G., Hauswirth, W. W., and Bennett, J. Gene therapy restores vision in a canine model of childhood blindness. *Nat Genet 28*, 1 (2001), 92–95.

[2] Adams, N. A., Awadein, A., and Toma, H. S. The retinal ciliopathies. *Ophthalmic Genet 28*, 3 (2007), 113–125.

[3] Apollo, N., Grayden, D. B., Burkitt, A. N., Meffin, H., and Kameneva, T. Modeling intrinsic electrophysiology of AII amacrine cells: preliminary results. *Conf Proc IEEE Eng Med Biol Soc 2013* (2013), 6551–6554.

[4] Bazhenov, M., Timofeev, I., Frohlich, F., and Sejnowski, T. Cellular and network mechanisms of electrographic seizures. *Drug Discov Today Dis Models 5*, 1 (2008), 45–57.

[5] Bazhenov, M., Timofeev, I., Steriade, M., and Sejnowski, T. Spiking-bursting activity in the thalamic reticular nucleus initiates sequences of spindle oscillations in thalamic networks. *J. Neurophysiol 84* (2000), 1076–1087.

[6] Benes, G., Barry, A. M., Kaper, T. J., Kramer, M. A., and Burke, J. An elementary model of torus canards. *Chaos 21* (2011), 023131.

[7] Bi, A., Cui, J., Ma, Y.-P., Olshevskaya, E., Pu, M., Dizhoor, A., and Pan, Z.-H. Ectopic expression of a microbial-type rhodopsin restores visual responses in mice with photoreceptor degeneration. *Neuron 50*, 1 (2006), 23–33.

[8] Bloomfield, S. A., Xin, D., and Osborne, T. Light-induced modulation of coupling between aii amacrine cells in the rabbit retina. *Vis Neurosci 14*, 3 (1997), 565–576.

[9] Borowska, J., Trenholm, S., and Awatramani, G. B. An intrinsic neural oscillator in the degenerating mouse retina. *J Neuroscience 31*, 13 (2011), 5000–5012.

[10] Burke, J., Desroches, M., Barry, A. M., Kaper, T. J., and Kramer, M. A. A showcase of torus canards in neuronal bursters. *J Math Neurosci 2* (2012), 3.

[11] Busskamp, V., Duebel, J., Balya, D., Fradot, M., Viney, T., Siegert, S., Groner, A., Cabuy, E., Forster, V.and Seeliger, M., Biel, M., Humphries, P., Paques, M., Mohand-Said, S., Trono, D., Deisseroth, K., Sahel, J., Picaud, S., and Roska, B. Genetic reactivation of cone photoreceptors restores visual responses in retinitis pigmentosa. *Science 329*, 5990 (2010), 413–417.

[12] Canavier, C. C., Baxter, D. A., Clark, J. W., and Byrne, J. H. Nonlinear dynamics in a model neuron provide a novel mechanism for transient synaptic inputs to produce long-term alterations of postsynaptic activity. *J Neurophysiol 69*, 6 (Jun 1993), 2252–2257.

[13] Carter-Dawson, L. D., LaVail, M. M., and Sidman, R. L. Differential effect of the rd mutation on rods and cones in the mouse retina. *Invest Ophthalmol Vis Sci 17*, 6 (1978), 489–498.

[14] Cembrowski, M. S., Logan, S. M., Tian, M., Jia, L., Li, W., Kath, W. L., Riecke, H., and Singer, J. H. The mechanisms of repetitive spike generation in an axonless retinal interneuron. *Cell Reports 1*, 2 (2012), 155–166.

[15] Chang, B., Hawes, N. L., Hurd, R. E., Davisson, M. T., Nusinowitz, S., and Heckenlively, J. R. Retinal degeneration mutants in the mouse. *Vision Res 42*, 4 (2002), 517–525.

[16] Chang, B., Hawes, N. L., Pardue, M. T., German, A. M., Hurd, R. E., Davisson, M. T., Nusinowitz, S., Rengarajan, K., Boyd, A. P., Sidney, S. S., Phillips, M. J., Stewart, R. E., Chaudhury, R., Nickerson, J. M., Heckenlively, J. R., and Boatright, J. H. Two mouse retinal degenerations caused by missense mutations in the beta-subunit of rod cGMP phosphodiesterase gene. *Vision Res 47*, 5 (2007), 624–633.

[17] Choi, H., Zhang, L., Cembrowski, M., Sabottke, C., Markowitz, A., Butts, D. A., Kath, W. L., Singer, J. H., and Riecke, H. Intrinsic bursting of AII amacrine cells underlies oscillations in the rd1 mouse retina. *J Neurophysiology (accepted)* (2014).

[18] Cymbalyuk, G., and Shilnikov, A. Coexistence of tonic spiking oscillations in a leech neuron model. *J Comput Neurosci 18*, 3 (2005), 255–263.

[19] Dacheux, R. F., and Raviola, E. The rod pathway in the rabbit retina: a depolarizing bipolar and amacrine cell. *J Neurosci 6*, 2 (1986), 331–345.

[20] Demb, J. B., and Singer, J. H. Intrinsic properties and functional circuitry of the AII amacrine cell. *Visual neuroscience 29* (2012), 51–60.

[21] Fenichel, F. Geometric singular perturbation theory for ordinary differential equations. *J. Differ. Equ. 31* (1979), 53–98.

[22] Field, G., and Rieke, F. Nonlinear signal transfer from mouse rods to bipolar cells and implications for visual sensitivity. *Neuron 34*, 5 (2002), 773–785.

[23] Field, G. D., Sampath, A. P., and Rieke, F. Retinal processing near absolute threshold: from behavior to mechanism. *Annu Rev Physiol 67* (2005), 491–514.

[24] Fine, I., Wade, A., Brewer, A., May, M., Goodman, D., Boynton, G., Wandell, B., and MacLeod, D. Long-term deprivation affects visual perception and cortex. *Nat Neurosci 6*, 9 (2003), 915–916.

[25] Fitzhugh, R. Impulses and physiological states in theoretical models of nerve membrane. *Biophys J 1*, 6 (1961), 445–466.

[26] Freed, M. A. Parallel cone bipolar pathways to a ganglion cell use different rates and amplitudes of quantal excitation. *J Neurosci 20*, 11 (2000), 3956–3963.

[27] Frohlich, F., and Bazhenov, M. Coexistence of tonic firing and bursting in cortical neurons. *Phys Rev E Stat Nonlin Soft Matter Phys 74* (2006), 031922.

[28] Grimes, W. N., Li, W.and Chavez, A. E., and Diamond, J. S. Bk channels modulate pre- and postsynaptic signaling at reciprocal synapses in retina. *Nat Neurosci 12*, 5 (2009), 585–592.

[29] Habermann, C., O'Brien, B., Wassle, H., and Protti, D. AII amacrine cells express L-type calcium channels at their output synapses. *J Neurosci 23*, 17 (2003), 6904–6913.

[30] Hack, I., Peichl, L., and Brandstatter, J. H. An alternative pathway for rod signals in the rodent retina: rod photoreceptors, cone bipolar cells, and the localization of glutamate receptors. *Proc Natl Acad Sci U S A 96*, 24 (1999), 14130–14135.

[31] Hartong, D. T., Berson, E. L., and Dryja, T. P. Retinitis pigmentosa. *Lancet 368*, 9549 (2006), 1795–1809.

[32] Hounsgaard, J., and Kiehn, O. Serotonin-induced bistability of turtle motoneurones caused by a nifedipine-sensitive calcium plateau potential. *J Physiol 414* (1989), 265–282.

[33] Izhikevich, E. Neural excitability, spiking, and bursting. *International Journal for Bifurcation and Chaos 10* (2000), 1171–1266.

[34] Izhikevich, E. *Dynamical Systems in Neuroscience:The Geometry of Excitability and Bursting*. MIT Press, 2005.

[35] Jimenez, A. J., Garcia-Fernandez, J. M., Gonzalez, B., and Foster, R. G. The spatio-temporal pattern of photoreceptor degeneration in the aged rd/rd mouse retina. *Cell Tissue Res 284*, 2 (1996), 193–202.

[36] Kaneko, Y., and Watanabe, S.-I. Expression of nav1.1 in rat retinal aii amacrine cells. *Neurosci Lett 424*, 2 (2007), 83–88.

[37] Lagali, P., Balya, D., Awatramani, G., Munch, T., Kim, D., Busskamp, V., Cepko, C., and Roska, B. Light-activated channels targeted to ON bipolar cells restore visual function in retinal degeneration. *Nat Neurosci 11*, 6 (2008), 667–675.

[38] Lechner, H. A., Baxter, D. A., Clark, J. W., and Byrne, J. H. Bistability and its regulation by serotonin in the endogenously bursting neuron r15 in aplysia. *J Neurophysiol 75*, 2 (1996), 957–962.

[39] Lin, B., Koizumi, A., Tanaka, N., Panda, S., and Masland, R. Restoration of visual function in retinal degeneration mice by ectopic expression of melanopsin. *Proc Natl Acad Sci U S A 105*, 41 (2008), 16009–16014.

[40] Ma, Y.-P., and Pan, Z.-H. Spontaneous regenerative activity in mammalian retinal bipolar cells: roles of multiple subtypes of voltage-dependent Ca^{2+} channels. *Vis Neurosci 20*, 2 (2003), 131–139.

[41] MacLaren, R. E., Pearson, R. A., MacNeil, A., Douglas, R. H., Salt, T. E., Akimoto, M., Swaroop, A., Sowden, J. C., and Ali, R. R. Retinal repair by transplantation of photoreceptor precursors. *Nature 444*, 7116 (2006), 203–207.

[42] Marc, R. E., Jones, B. W., Anderson, J. R., Kinard, K., Marshak, D. W., Wilson, J. H., Wensel, T., and Lucas, R. J. Neural reprogramming in retinal degeneration. *Investigative ophthalmology & visual science 48* (2007), 3364–3371.

[43] Marc, R. E., Jones, B. W., Watt, C. B., and Strettoi, E. Neural remodeling in retinal degeneration. *Prog Retin Eye Res 22*, 5 (2003), 607–655.

[44] Margolis, D. J., and Detwiler, P. B. Different mechanisms generate maintained activity in on and off retinal ganglion cells. *J Neurosci 27*, 22 (2007), 5994–6005.

[45] Margolis, D. J., Gartland, A. J., Singer, J. H., and Detwiler, P. B. Network oscillations drive correlated spiking of ON and OFF ganglion cells in the rd1 mouse model of retinal degeneration. *PLoS ONE 9*, 1 (2014), e86253.

[46] Margolis, D. J., Newkirk, G., Euler, T., and Detwiler, P. B. Functional stability of retinal ganglion cells after degeneration-induced changes in synaptic input. *J Neurosci 28*, 25 (2008), 6526–6536.

[47] Menzler, J., and Zeck, G. Network oscillations in rod-degenerated mouse retinas. *J Neurosci 31*, 6 (2011), 2280–2291.

[48] Murphy, G., and Rieke, F. Network variability limits stimulus-evoked spike timing precision in retinal ganglion cells. *Neuron 52*, 3 (2006), 511–524.

[49] Nelson, R. Cat cones have rod input: a comparison of the response properties of cones and horizontal cell bodies in the retina of the cat. *J Comp Neurol 172*, 1 (1977), 109–135.

[50] Nirenberg, S., and Pandarinath, C. Retinal prosthetic strategy with the capacity to restore normal vision. *Proc Natl Acad Sci U S A 109*, 37 (2012), 15012–15017.

[51] Pan, F., Mills, S. L., and Massey, S. C. Screening of gap junction antagonists on dye coupling in the rabbit retina. *Vis Neurosci 24*, 4 (2007), 609–618.

[52] Pontryagin, L., and Rodygin, L. Periodic solution of a system of ordinary differential equations with a small parameter in the terms containing derivatives. *Sov. Math. Dokl 1* (1960), 611–619.

[53] Sampath, A. P., and Rieke, F. Selective transmission of single photon responses by saturation at the rod-to-rod bipolar synapse. *Neuron 41*, 3 (2004), 431–443.

[54] Schneeweis, D. M., and Schnapf, J. L. Photovoltage of rods and cones in the macaque retina. *Science 268*, 5213 (1995), 1053–1056.

[55] Shilnikov, A. Complete dynamical analysis of a neuron model. *Nonlin Dyn 68* (2012), 305–328.

[56] Shilnikov, A., Calabrese, R. L., and Cymbalyuk, G. Mechanism of bistability: tonic spiking and bursting in a neuron model. *Phys Rev E Stat Nonlin Soft Matter Phys 71* (2005), 056214.

[57] Shilnikov, A., and Cymbalyuk, G. Transition between tonic spiking and bursting in a neuron model via the blue-sky catastrophe. *Phys Rev Lett 94* (2005), 048101.

[58] Smith, R. G., and Vardi, N. Simulation of the AII amacrine cell of mammalian retina: functional consequences of electrical coupling and regenerative membrane properties. *Vis Neurosci 12*, 5 (1995), 851–860.

[59] Soucy, E., Wang, Y., Nirenberg, S., Nathans, J., and Meister, M. A novel signaling pathway from rod photoreceptors to ganglion cells in mammalian retina. *Neuron 21*, 3 (1998), 481–493.

[60] Stasheff, S. F. Emergence of sustained spontaneous hyperactivity and temporary preservation of OFF responses in ganglion cells of the retinal degeneration (rd1) mouse. *J Neurophysiology 99*, 3 (2008), 1408–1421.

[61] Steriade, M., McCormick, D., and Sejnowski, T. Thalamocortical oscillations in the sleeping and aroused brain. *Science 262* (1993), 679–685.

[62] Stingl, K., Bartz-Schmidt, K., Besch, D., Braun, A., Bruckmann, A., Gekeler, F., Greppmaier, U., Hipp, S., Hortdorfer, G., Kernstock, C., Koitschev, A., Kusnyerik, A., Sachs, H., Schatz, A., Stingl, K., Peters, T., Wilhelm, B., and Zrenner, E. Artificial vision with wirelessly powered subretinal electronic implant alpha-IMS. *Proc Biol Sci 280*, 1757 (2013), 20130077.

[63] Terman, D. Chaotic spikes arising from a model of bursting in excitable membranes. *SIAM J Appl Math 51* (1991), 1418–1450.

[64] Terman, D. The transition from bursting to continuous spiking in excitable membrane models. *J Nonlinear Sci 2* (1992), 135–182.

[65] Terman, D., Rubin, J., Yew, A., and Wilson, C. Activity patterns in a model for the subthalamopallidal network of the basal ganglia. *J. Neurosci 22* (2002), 2963–2976.

[66] Tian, M., Jarsky, T., Murphy, G. J., Rieke, F., and Singer, J. H. Voltage-gated Na channels in AII amacrine cells accelerate scotopic light responses mediated by the rod bipolar cell pathway. *J Neuroscience 30*, 13 (2010), 4650–4659.

[67] Toychiev, A. H., Ivanova, E., Yee, C. W., and Sagdullaev, B. T. Block of gap junctions eliminates aberrant activity and restores light responses during retinal degeneration. *J Neuroscience 33*, 35 (Aug 2013), 13972–13977.

[68] Trenholm, S., Borowska, J., Zhang, J., Hoggarth, A., Johnson, K., Barnes, S., Lewis, T., and Awatramani, G. Intrinsic oscillatory activity arising within the electrically-coupled AII amacrine/ON cone bipolar cell network is driven by voltage-gated Na^+ channels. *J Physiology 590* (2012), 2501–2517.

[69] Turrigiano, G. G., Marder, E., and Abbott, L. F. Cellular short-term memory from a slow potassium conductance. *J Neurophysiol 75* (1996), 963–966.

[70] van Wyk, M., Wassle, H., and Taylor, W. R. Receptive field properties of ON- and OFF-ganglion cells in the mouse retina. *Vis Neurosci 26*, 3 (2009), 297–308.

[71] Veruki, M. L., and Hartveit, E. AII (Rod) amacrine cells form a network of electrically coupled interneurons in the mammalian retina. *Neuron 33*, 6 (2002), 935–946.

[72] Veruki, M. L., and Hartveit, E. Electrical synapses mediate signal transmission in the rod pathway of the mammalian retina. *J Neurosci 22*, 24 (2002), 10558–10566.

[73] Weiland, J. D., Liu, W., and Humayun, M. S. Retinal prosthesis. *Annu Rev Biomed Eng 7* (2005), 361–401.

[74] Wojcik, J., and Shilnikov, A. Voltage interval mappings for activity transitions in neuron models for elliptic bursters. *Physica D 240* (2011), 1164–1180.

[75] Wu, S.-N., Hsu, M.-C., Liao, Y.-K., Wu, F.-T., Jong, Y.-J., and Lo, Y.-C. Evidence for inhibitory effects of flupirtine, a centrally acting analgesic, on delayed rectifier K^+ currents in motor neuron-like cells. *Evid Based Complement Alternat Med 2012* (2012), 148403.

[76] Ye, J. H., and Goo, Y. S. The slow wave component of retinal activity in rd/rd mice recorded with a multi-electrode array. *Physiol Meas 28*, 9 (2007), 1079–1088.

[77] Yee, C. W., Toychiev, A. H., and Sagdullaev, B. T. Network deficiency exacerbates impairment in a mouse model of retinal degeneration. *Frontiers in Systems Neuroscience 6* (2012).

[78] Zenisek, D., and Matthews, G. Calcium action potentials in retinal bipolar neurons. *Vis Neurosci 15*, 1 (1998), 69–75.